Identifying Dynamic Stall Effects on the Pitching Moment From Cessna Citation II Flight Test Data

van Wezel, Casper; Pool, D.M.; de Visser, C.C.

DOI
10.2514/6.2025-1252

Publication date
2025

Document Version
Final published version

Published in
Proceedings of the AIAA SCITECH 2025 Forum

AIAA SciTech Forum
6-10 January 2025, Orlando, FL
AIAA SCITECH 2025 Forum

10.2514/6.2025-1252

A Nonlinear Unsteady Pitching Moment Stall Model from Cessna Citation II Flight Test Data

C.J. van Wezel*, D.M. Pool † and C.C. de Visser‡
Delft University of Technology, 2600 GB Delft, The Netherlands

One of the most widely applied identification methods for stall modeling using flight test data is based on Kirchhoff's method of flow separation. However, this approach has not lead to a satisfactory aerodynamic pitching moment model. The introduction of the so-called X-variable, representing the point of flow separation on the wing, interferes with identification of a pitch damping term, that is required for dynamic stability. In general, Kirchhoff methods lead to models that are incompatible with nominal flight envelope models. This paper presents a nonlinear unsteady model of the pitching moment using lag states of the angle of attack measurements, identified from flight test data collected with a Cessna Citation II laboratory aircraft. The model is formulated in terms of well-known stability derivatives and is a one-on-one extension of the nominal envelope model. Model regressors are selected from a large pool of candidates using Multivariate Orthogonal Function Modeling. The candidate pool is based on a newly formulated mathematical model, such that each model contribution has a clear physical interpretation. The model has good predictive abilities and results in a reduction of 55.9% in validation MSE compared to Kirchhoff based pitching moment models.

I. Nomenclature

Roman

A_*	Specific force in -direction [m/s^2]	S	Wing surface [m^2]
$\overline{b}$	Wing span [-]	$\overline{S}_T$	Tail to Wing surface ratio [-]
$\overline{c}$	Mean aerodynamic chord [-]	t	Time [s]
C_*	Aerodynamic force/moment coefficient [-]	u	Step function
C_{m_*}	Aerodynamic pitching moment derivative w.r.t. *	$\overline{V}_T$	Tail to wing airspeed ratio [-]
C_{L_*}	Aerodynamic lift derivative w.r.t. *	V_∞	Free stream air speed [m/s]
F_e	Earth-fixed reference frame	V_{TAS}	True air speed [m/s]
h	Altitude [m]	V_{stall}	Stall speed
I_*	Mass moment of inertia about *-axis [kgm^2]	X	Point of flow separation variable [-]
$\overline{L}_T$	Tail moment arm [-]	$\mathbf{x}$	Physical regressor vector
m	Mass [kg]	x	Spline knot
N	Number of samples	x_e, y_e, z_e	Cartesian position in F_e [m]
n	Number of model terms	x^W	Wing lift moment arm [-]
$\mathbf{p}$	Orthogonalized regressor vector	$\mathbf{y}$	Measurement vector
p	Roll rate [rad]	$\hat{\boldsymbol{y}}$	Model output vector
q	Pitch rate [rad]	y	Spline knot
r	Yaw rate [rad]		

Greek

α	Angle of attack [rad]	δ	Control surface deflection [rad]
α_{t-k}	kth sample angle of attack lag state	ε	Downwash at tail [rad]
Γ	Transformation matrix	$\boldsymbol{\theta}$	Physical parameter vector
$\gamma_{k,j}$	Gram-Schmidt scaling parameter	θ	Pitch angle [rad]

*M.Sc. student, Control and Simulation Division, Faculty of Aerospace Engineering, P.O. Box 5058, The Netherlands; c.j.vanwezel@tudelft.nl
†Assistant Professor, Control & Simulation Section, Faculty of Aerospace Engineering, P.O. Box 5058; d.m.pool@tudelft.nl. Associate Fellow AIAA.
‡Associate Professor, Control & Simulation Section, Faculty of Aerospace Engineering, P.O. Box 5058; c.c.devisser@tudelft.nl. Member AIAA.

σ	Standard deviation	ϕ	Bank angle [rad]
τ_*	Time lag with index *	ψ	Heading angle [rad]
$\boldsymbol{\phi}$	Orthogonal parameter vector		

Subscripts

0	Constant contribution/steady state	e	Elevator
1	Nominal flight contribution/amplitude	L	Lift force
2	Stall contribution	m	Pitching moment
+	Spline	T	Thrust force
d	Dynamic		

Superscripts

T	Tail	$\circ$	Degrees
W	Wing	$\intercal$	Transpose
B	Body		

II. Introduction

Loss of control in flight (LOC-I) is the most common cause of fatal accidents in civil and general aviation, and the main contributor is aerodynamic stall [1]. Therefore, flight simulator-based stall prevention and recovery training has become obligatory in the US [2] per 2019. Similar legislation was passed in the European Union [3]. Simulator based training requires stall models [4]. This gives rise to an increased demand in accurate stall models for aircraft.

Stall is a highly nonlinear and unsteady flight condition [5]. Conventional aircraft models, that are based on the stability derivative concept, are incapable of modeling unsteady nonlinear aerodynamics [6–8]. Therefore, Goman et al. [8, 9] and Klein et al. [10, 11] model the aerodynamic parameters as function of oscillation frequency and amplitude using forced-oscillation data from wind tunnel experiments. This approach leads to parameterized look up tables that are only applicable to forced oscillations. Moreover, this experimental data lacks control inputs. A model fit for simulators should only include universal aircraft states, including control variables, and be valid for arbitrary motion. This is what models identified from flight test data can provide.

In a previous research effort, a longitudinal model was presented by van Ingen et al. [12] based on Kirchhoff's theory of flow separation. These type of models make use of the internal state variable X, that represents the point of flow separation on the wing [13]. By means of this same method, Wang et al. presented a longitudinal model with higher order X-terms to resolve issues with, amongst other things, the pitching moment model. Although it was found that such models provides an accurate fit, it comes with a number of drawbacks. Firstly, the X-variable is a synthetic state that cannot be directly measured but needs to be computed post-flight through a nonlinear optimization that is based on a phenomenological relationship. Secondly, the current stall models are local, and in general incompatible with nominal (global) flight models that consist of the familiar control and stability derivatives. Thirdly, obtaining physically accurate pitch damping with Kirchhoff's theory based stall models turns out to be problematic. The inclusion of the X-variable interferes with the identification of a pitch damping coefficient that is required for dynamic stability. In addition, the X-variable has limited physical meaning with respect to the pitching moment because flow separation only partly explains its dynamic behavior. In reality it is a combination of flow separation, moving center of pressure (COP) on the wing [14–16] and downwash lag at the tail [17–19]. Finally, model error may arise from the fact that the X-variable is a bounded variable. It varies between 0 (full flow separation) and 1 (fully attached flow). As a result, after the point of full flow separation, this regressor is reduced to a constant and can no longer represent the aerodynamics that continue to develop even after flow separation.

This paper aims to provide an alternative to the Kirchhoff based modeling of the pitching moment. Data from stall maneuvers excited with quasi-random inputs where obtained during flight tests with the Cessna Citation II laboratory aircraft (PH-LAB) operated by the Delft University of Technology (TUD) and the Netherlands Aerospace Centre (NLR). A novel mathematical pitching moment model is derived that includes all aspects of the pitching moment in nominal and stalled flight. Based on this mathematical model, a large set of circa 100 candidate regressors terms is generated. These include lag states of the angle of attack to model the combined effect of flow separation and moving COP, and univariate splines to model nonlinear pitch and downwash lag damping. Multivariate Orthogonal Function (MOF) [20, 21] modeling is then used to identify the most relevant model contributions.

The structure of this paper is as follows: section III provides an overview of various unsteady aspects that need to be taken into account in the pitching moment model. In section IV a new mathematical model formulation is presented. section V discusses the flight test data and section VI the methodology. Then the results are presented in section VII and finally a conclusion is found in section VIII.

III. Dynamic Stall Characteristics

Dynamic stall refers to the delay of steady stall beyond the static stall angle of attack on airfoils and wings under unsteady motion [22]. Such unsteady motions include pitching, plunging and heaving. In the subsequent only pitching motions are considered. During dynamic stall, a series of aerodynamic phenomena can be observed, that each have a pronounced effect on the aerodynamic forces and moments [16, 23]. This is discussed in subsection III.A. Furthermore, subsection III.B talks about two different stall types. Lastly, subsection III.C explains how the interaction between wing and tail contributes to dynamic stall.

A. Stages of Dynamic Stall

Figure 1 shows an illustration of what an unsteady lift curve can look like for an airfoil undergoing a pitching motion with a constant angle of attack rate. This illustration is of the hand of Choudhry et al. [23], and they identify 6 stages of dynamic stall:

1) On the onset of rotation, the lift curve closely follows the steady-state curve, although a slight offset can be observed that indicates the first effects of dynamic stall.
2) A regime follows that is characterized by a near linear lift slope past the point of steady stall. The reach of this regime is related to the angle of attack rate. This phenomenon can be explained by the formation of a vortex at the trailing edge, providing additional suction pressure, keeping the flow attached. Another explanation is the so called *leading edge jet effect*.
3) Next, a flat portion appears, referred to as the plateau. At this stage, separation has initiated at the trailing edge and moves towards the leading edge. Meanwhile, a separation bubble forms at the leading edge.
4) The plateau is an indication for the formation of a large vortex at the leading edge (LE), the dynamic stall vortex (DSV). Immediately following the plateau, a sharp rise in lift is observed. This increase is the direct result of the formation and shedding of the DSV. The DSV rolls over the wing, increasing lift momentarily. When the DSV 'spills', it moves aft, resulting in a displacement of the center of pressure (COP) in the same direction.
5) The DSV has convected to mid-chord, where the maximum lift is achieved. At this point the DSV leaves the airfoil surface.
6) Now the post-stall domain is entered, where the wing experiences a dramatic drop in lift.

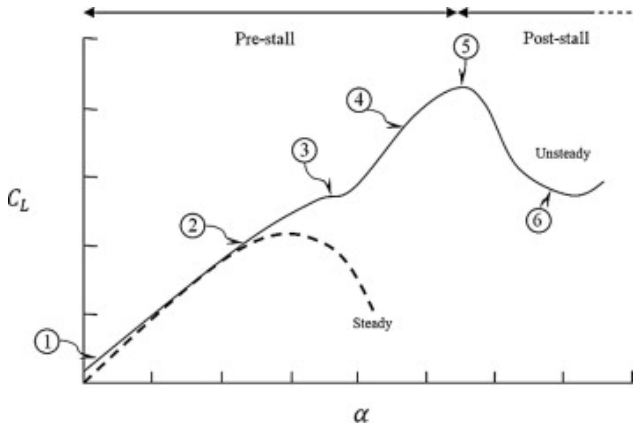

Fig. 1 Comparison of unsteady and steady-state primary lift-curve undergoing unsteady ramp-type dynamic stall. This illustration was taken from Choudhry et al. [23].

Especially the formation and the subsequent shedding of the leading edge vortex has dramatic effects on the lift, drag and pitching moment. In its final act, the DSV causes a sharp peak in the lift force. During this event, the COP

of the wing moves aft. The combination of the increased lift force and moment arm leads to a strong increase in the negative pitching moment. This phenomenon is referred to as the *moment stall* [14, 16, 23]. The instant where the DSV has separated and the lift finally decreases is referred to as the *lift stall*. The moment stall precedes the lift stall and the delay between the two can be related to the velocity at which the DSV convects over the wing [24]. Although not shown in Figure 1, additional secondary and even tertiary vortices can appear on the wing, leading to further lift, drag and pitching moment peaks [14].

B. Stall Degree

Two types of stall can be distinguished in pitching airfoils, being light and deep stall. In light stall, the maximum angle of attack and lift stall more or less coincide. In deep stall, the maximum angle of attack is increased beyond the point of lift stall. Also, in light stall the DSV is not fully developed, while it is in deep stall [25]. As a result the load-peaks in deep stall reach significantly larger values. The type of stall can be clearly recognized from the moment hysteresis curves. Figure 2a and 2b illustrate the moment hysteresis for light and deep stall respectively.

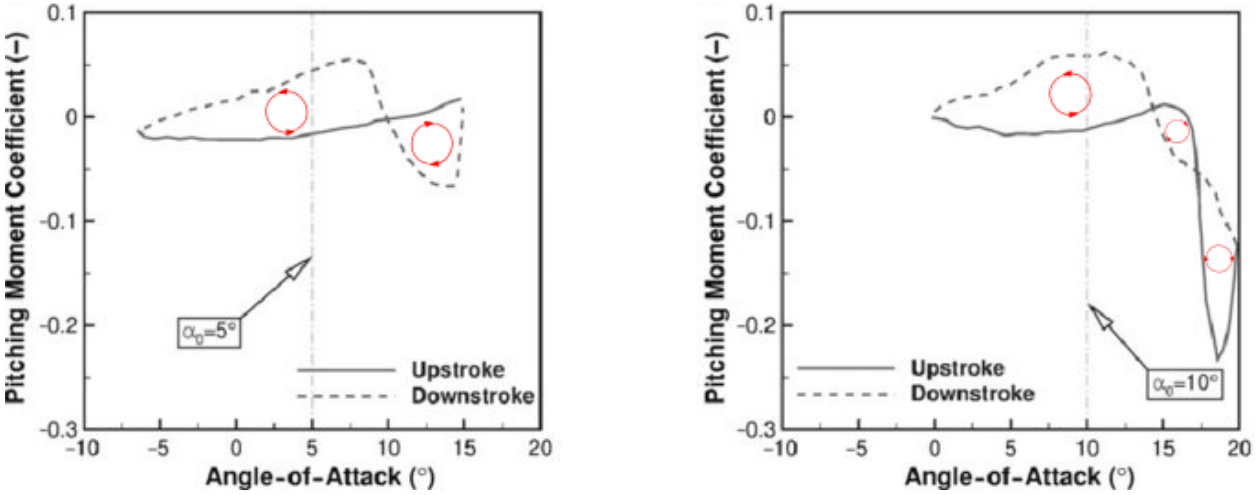

Fig. 2 Typical pitch moment coefficient hysteresis curves for (a) light stall and (b) deep stall for a NACA0012 airfoil in pitch oscillation, each with a different mean angle of attack (α_0), but the same amplitude and frequency. These illustrations were taken from McCroskey et al. [25].

It is observed that the aerodynamic damping in stall can become unstable, implying the pitching motion amplifies instead of dampening [26, 27]. This stall induced unstable damping is found in clockwise moment hysteresis loops, i.e. where the pitching moment is higher on the upstroke than on the downstroke [16, 24]. According to Corke et al. the amount of damping, whether positive or negative, is related to the size of the moment hysteresis loops. McCroskey et al. noted that light stall is more aerodynamically unstable than deep stall [25]. And indeed, Figure 2a and b reveal that the light stalls have a larger clockwise loop.

Figure 2a and b are a good illustration of the consequences of unsteady aerodynamics on the pitching moment. A comparison of points on the two curves reveals that the instantaneous angle of attack alone is insufficient to predict the corresponding pitching moment; the motion's prehistory also plays a significant role. For instance, at an angle of attack of 10° on the downstroke phase, the pitching moment value and its slope with respect to angle of attack differ substantially between the two motions. In Figure 2b, the motion has largely recovered from stall (note that this point lies in the large, left most counter clockwise loop). In contrast, the motion in Figure 2a is still in the recovery phase, characterized by a steep positive slope. These differences are attributable to the influence of motion prehistory.

The distinct angle-of-attack regimes of these two motions might obscure some of the more striking effects of motion history on the pitching moment. To illustrate this point, Ericsson and Reding [24] draw on wind tunnel data from Carr et al. [28], demonstrating that even for motions with identical angle-of-attack ranges but varying frequencies, a wide range of pitching moment dynamics can be observed.

C. Wing Tail Interaction

The literature discussed in subsection III.A and III.B exclusively looked at airfoils in unsteady motion. An aircraft with a wing-tail configuration has an additional source of unsteadiness. This stems from the interaction between wing and tail [17, 18, 29]. The wing causes the free stream flow to deflect downwards, which results in a downwash ε at the tail. The downwash is a function of the wing angle of attack and assumed to be linear in attached flow. An instantaneous change in wing angle of attack will not be instantly reflected in the tail downwash. Instead, the modified flow resulting from this change in angle of attack reaches the tail with a time lag. This lag approximately amounts to the time needed for the flow to travel from the trailing edge of the wing to the tail surface. The downwash lag can be proportionally related to the angle of attack rate in a first order approximation, effectively resulting in a quasi-steady effect rather than an unsteady effect. Just like pitch damping, the downwash lag provides aerodynamic damping.

IV. Mathematical Modeling of Pitching Moment

A standard formulation of the aircraft control and stability derivatives results from a Taylor series expansion around a trim point with only first order (linear) terms retained [29]. However, a first order model is only valid in the nominal flight envelope where nonlinear and unsteady effects are negligible around the trim point. In a nonlinear unsteady regime, such a model is inadequate. In the subsequent, the classical linear steady mathematical formulation and a nonlinear unsteady mathematical model by Khrabrov et al. [15] for the pitching moment are discussed in subsection IV.A and subsection IV.B, respectively. Then, the novel model formulation for the pitching moment is presented in subsection IV.C, that encompasses both linear steady and nonlinear unsteady aerodynamics.

A. Mathematical Modeling of Linear Steady Pitching Moment

The classical first order Taylor expansion in terms of the aircraft states and control variables is given by Equation 1.

$$C_m = C_{m_0} + C_{m_\alpha}\alpha + C_{m_q} q + C_{m_{\dot\alpha}}\dot\alpha + C_{m_{\delta_e}}\delta_e \tag{1}$$

Where only the angle of attack α, pitch rate q, angle of attack rate $\dot\alpha$ and elevator deflection δ_e are considered to effect the pitching moment. The variation with altitude and velocity are excluded, assuming a single flight condition. The stability derivatives C_{m_α}, C_{m_q} and $C_{m_{\dot\alpha}}$ can be broken down into equations Equation 2-4. A derivation is provided in e.g. [29].

$$C_{m_\alpha} = -C_{L_\alpha} x^W - C^T_{L_\alpha}(1 - \frac{\partial\varepsilon}{\partial\alpha})\overline{V}^2_T \overline{S}_T \overline{L}_T \tag{2}$$

$$C_{m_q} = \frac{\partial C^T_L}{\partial\alpha}\overline{V}^2_T \overline{S}_T \overline{L}^2_T \tag{3}$$

$$C_{m_{\dot\alpha}} = \frac{\partial C^T_L}{\partial\alpha}\frac{\partial\varepsilon}{\partial\alpha}\overline{V}^2_T \overline{S}_T \overline{L}^2_T \tag{4}$$

In Equation 2-4 $\overline{V}_T$ is the ratio of the airspeed at the tail and wing which is assumed to be constant. $\overline{S}_T$ is the tail to wing surface ratio, and $\overline{L}_T$ the tail arm normalized by the mean aerodynamic chord (MAC) $\overline{c}$. The superscripts W and T indicate the wing and tail respectively. C_{L_α} is the lift gradient and $\frac{\partial\varepsilon}{\partial\alpha}$ the downwash gradient. C_{m_α} represents the moment generated by the wing and tail at a certain α. C_{m_q} is the additional pitching moment in a pure pitch motion generated at the tail due to curvature of the air around the center of gravity (CG). Here the contribution by the wing is neglected. Furthermore, $C_{m_{\dot\alpha}}$ is the downwash lag coefficient and it represents the quasi-steady effect described in subsection III.C.

Due to the tight kinematic coupling between q and $\dot\alpha$, the pitch damping and downwash lag coefficient are oftentimes combined into one parameter. Since $q \simeq \dot\alpha$ the following can be derived:

$$C^*_{m_q} = C_{m_q} + C_{m_{\dot\alpha}} = \frac{\partial C^T_L}{\partial\alpha}(1 + \frac{\partial\varepsilon}{\partial\alpha})\overline{V}^2_T \overline{S}_T \overline{L}^2_T \tag{5}$$

resulting in the simplified model in Equation 6.

$$C_m = C_{m_0} + C_{m_\alpha}\alpha + C^*_{m_q} q + C_{m_{\delta_e}}\delta_e \tag{6}$$

B. TsAGI Model

Khrabrov et al. proposed a mathematical model formulation that can describe the nonlinear unsteady aerodynamics of the pitching moment of a conventional wing-tail-body configured aircraft, commonly referred to as the *TsAGI model* [15]:

$$\begin{aligned} &C_m = C_m^B(\alpha) + C_{m_0}^W + C_L^W x^W - \overline{L}_T \overline{S}_T C_L^T(\alpha + \alpha_d - \varepsilon) + C_{m_q}(\alpha) q \\ &\text{where:} \\ &\alpha_d = -\frac{\overline{L}_T \overline{c} q}{V_\infty} \end{aligned} \tag{7}$$

Where C_L^W and C_L^T are the wing and tail lift respectively, as indicated by the superscripts W and T. C_m^B is a moment generated by the fuselage, x^W is the distance from the COP of the wing to the CG of the aircraft. Furthermore, α_d is an additional contribution to the angle of attack as seen by the tail caused by the aircraft rotating around its CG. $C_{m_q}(\alpha)$ is a nonlinear pitch damping derivative. C_L^W is partitioned into two components:

$$C_L^W = C_{L1} + C_{L2} \tag{8}$$

Here C_{L1} represents the linear part of the wings' lift, associated with attached flow, and C_{L2} the deviation from linear lift, caused by flow separation. These equations do not describe unsteady aerodynamics, as all the terms are functions of the instantaneous angle of attack. However, according to Khrabrov et al, all of C_{L2}, x^W and ε are unsteady variables. To make Equation 7 valid in both steady and unsteady conditions, Khrabrov et al. introduce three ODEs, given by Equation 9-11.

$$\tau_1(\alpha)\frac{\partial C_{L2}}{\partial t} + C_{L2} = C_{L20}(\alpha) \tag{9}$$

$$\tau_2(\alpha)\frac{\partial x^W}{\partial t} + x^W = x_0^W(\alpha) \tag{10}$$

$$\tau_3(\alpha)\frac{\partial \varepsilon}{\partial t} + \varepsilon = \varepsilon_0(\alpha) \tag{11}$$

$\tau_1(\alpha)$, $\tau_2(\alpha)$ and $\tau_3(\alpha)$ are three time lags that depend on the angle of attack, and $C_{L20}(\alpha)$, $x_0^W(\alpha)$ and $\varepsilon_0(\alpha)$ are three nonlinear functions that describe the steady behavior of the three unsteady variables. Note that Equations 7-11 require the identification of 7 nonlinear functions, being $C_{m_q}(\alpha)$, $\tau_1(\alpha)$, $\tau_2(\alpha)$, $\tau_3(\alpha)$, $C_{L20}(\alpha)$, $x_0^W(\alpha)$ and $\varepsilon_0(\alpha)$. Khrabrov et al. were able to do so by means of wind tunnel tests using experiments with different configuration of the test aircraft (e.g. only body and wing or only body and tail). However, in flight testing it is not possible to obtain data sets for different body configurations. Consequently, all the above described functions would need to be estimated from a single data set where effects due to wing, tail, body and their interactions are coupled, which may not be achievable given realistic system identification procedures.

C. Modified Mathematical Pitching Moment Model

In order to turn Equation 7 into a form more suitable for identification from flight test data, it is first of all desirable to eliminate the ODEs in Equations 9-11. These ODEs effectively act as a time lag filter, such that the unsteady variables are not only a function of the instantaneous α, but also of that at previous time instances. This is how the prehistory of the angle of attack enters the model equations. Analogously, C_{L2} could also be directly modeled as a nonlinear function of the time trace of α, as in Equation 12.

$$\begin{aligned} C_L^W &= C_{L1}^W(\alpha) + C_{L2}^W(\alpha(t)) \\ &= C_{L0}^W + C_{L1\alpha}^W \alpha + C_{L2}^W(\alpha(t)) \end{aligned} \tag{12}$$

Here the attached flow component C_{L1} has been rewritten in terms of the parameters from the nominal model. Similarly, this trick can be applied to x^W, C_L^T and ε. This gives Equations 13-15.

$$
\begin{aligned}
x^W &= x_1^W + x_2^W(\alpha(t)) \\
&= x_0^W + \frac{\partial x_1}{\partial \alpha}\alpha + x_2^W(\alpha(t)) \\
&\approx x_0^W + x_2^W(\alpha(t))
\end{aligned} \tag{13}
$$

$$
\begin{aligned}
C_L^T &= C_{L1}^T(\alpha) + C_{L2}^T(\alpha) \\
&= C_{L0}^T + C_{L1_\alpha}^T \alpha_T + C_{L2}^T(\alpha)
\end{aligned} \tag{14}
$$

where

$$\alpha_T = \alpha - \varepsilon$$

$$
\begin{aligned}
\varepsilon &= \varepsilon_1(\alpha) + \varepsilon_2(\alpha) \\
&= \varepsilon_0 + \frac{\partial \varepsilon_1}{\partial \alpha}\alpha + \varepsilon_2(\alpha)
\end{aligned} \tag{15}
$$

The subscripts 0 and 1 in Equations 12-15 always correspond to the linear steady aerodynamic contribution, such as those in nominal conditions. The subscript 2 refers to the deviation from these conditions, due to nonlinear and possibly unsteady aerodynamics. Note that $C_{L2}^T(\alpha)$ and $\varepsilon_2(\alpha)$ in Equations 14 and 15 are given as nonlinear steady functions, as evident by the omission of (t). The assumption that the tail lift is a steady function can be justified by the fact that flow separation is not likely to occur due to downwash reducing the effective angle of attack at the tail. The unsteadiness introduced by the downwash lag will be introduced later by including a $C_{m_{\dot{\alpha}}}$ parameter in addition to C_{m_q}.

Since $C_{L2}^T(\alpha)$ and $\varepsilon_2(\alpha)$ are steady correction functions for the linear dynamics, they must carry a value of zero up to some critical α. In the absence of a good model for the nonlinear tail lift and downwash contributions, they will be represented by a linear combination of spline basis functions in the subsequent:

$$
\begin{aligned}
&C_{L2}^T(\alpha) = \sum_{i=1}^{n} c_i(\alpha - x_i)_+^i \\
&\text{where:} \\
&(\alpha - x_i)_+^i = \begin{cases} (\alpha - x_i)^i & \text{if } \alpha \geq x_i \\ 0 & \text{if} \alpha < x_i \end{cases}
\end{aligned} \tag{16}
$$

$$
\begin{aligned}
&\varepsilon_2(\alpha) = \sum_{i=1}^{m} d_i(\alpha - y_i)_+^i \\
&\text{where:} \\
&(\alpha - y_i)_+^i = \begin{cases} (\alpha - y_i)^i & \text{if } \alpha \geq y_i \\ 0 & \text{if } \alpha < y_i \end{cases}
\end{aligned} \tag{17}
$$

c_i and d_i are to be determined coefficients, x_i and y_i are knots, and n and m are the highest order spline components included. Note that the lowest level contribution would be a first order term, i.e. $c_1(\alpha - x_1)_+$, representing a change of slope at $\alpha > x_1$.

Now we can write the contribution to the pitching moment in a pure α-motion using the expressions in Equation 12, 13 and 14:

$$
\begin{aligned}
C_m &= -C_L^W x^W - C_L^T \overline{V}_T^2 \overline{S}_T \overline{L}_T \\
&= -\left(C_{L1}^W(\alpha) + C_{L2}^W(\alpha(t))\right)\left(x_1^W + x_2^W(\alpha(t)\right) - \left(C_{L1}^T(\alpha) + C_{L2}^T(\alpha)\right)\overline{V}_T^2 \overline{S}_T \overline{L}_T \\
&= -C_{L1}^W(\alpha)x_1^W - C_{L1}^W(\alpha)x_2^W(\alpha(t)) - C_{L2}^W(\alpha(t))x_1^W - C_{L2}^W(\alpha(t))x_2^W(\alpha(t)) \\
&\quad - C_{L1}^T(\alpha)\overline{V}_T^2 \overline{S}_T \overline{L}_T - C_{L2}^T(\alpha)\overline{V}_T^2 \overline{S}_T \overline{L}_T
\end{aligned} \tag{18}
$$

Then the change in pitching moment with a change in the instantaneous α is given as:

$$\begin{aligned}
C_{m_\alpha} = &-\frac{\partial C^W_{L1}(\alpha)}{\partial \alpha} x^W_1 - \frac{\partial C^W_{L1}(\alpha)}{\partial \alpha} x^W_2(\alpha(t)) - C^W_{L1}(\alpha)\frac{\partial x^W_2(\alpha(t))}{\partial \alpha} \\
&- \frac{\partial C^W_{L2}(\alpha(t))}{\partial \alpha} x^W_1 - \frac{\partial C^W_{L2}(\alpha(t))}{\partial \alpha} x^W_2(\alpha(t)) - C^W_{L2}(\alpha(t))\frac{\partial x^W_2(\alpha(t))}{\partial \alpha} \\
&- \frac{\partial C^T_{L1}(\alpha)}{\partial \alpha}\overline{V}^2_T \overline{S}_T \overline{L}_T - \frac{\partial C^T_{L2}(\alpha)}{\partial \alpha}\overline{V}^2_T \overline{S}_T \overline{L}_T \\
= &-C^W_{L1_\alpha} x^W_0 - C^T_{L1_\alpha}\left(1 - \frac{\partial \varepsilon}{\partial \alpha}\right)\overline{V}^2_T \overline{S}_T \overline{L}_T \\
&- \frac{\partial C^W_{L1}(\alpha)}{\partial \alpha} x^W_2(\alpha(t)) - C^W_{L1}(\alpha)\frac{\partial x^W_2(\alpha(t))}{\partial \alpha} - \frac{\partial C^W_{L2}(\alpha(t))}{\partial \alpha} x^W_1 \\
&- \frac{\partial C^W_{L2}(\alpha(t))}{\partial \alpha} x^W_2(\alpha(t)) - C^W_{L2}(\alpha(t))\frac{\partial x^W_2(\alpha(t))}{\partial \alpha} - \frac{\partial C^T_{L2}(\alpha)}{\partial \alpha}\overline{V}^2_T \overline{S}_T \overline{L}_T \\
= &\, C_{m1_\alpha} + C_{m2_\alpha}(\alpha(t))
\end{aligned} \tag{19}$$

Now C_{m1_α} is identical to the α derivative of the linear steady model in Equation 2, while C_{m2_α} is a nonlinear unsteady function that models the effects on the pitching moment due to the nonlinear unsteady deviation of the linear lift caused by the wing stalling and potential nonlinear effects at the tail. As noted in subsection III.B, the slope of the pitching moment curve with respect to the angle of attack, evaluated at the instantaneous angle of attack, may vary depending on the motion prehistory of the aircraft. This is precisely what the contribution $C_{m2_\alpha}(\alpha(t))\alpha$ accounts for. It represents the unsteady pitching moment evaluated at the instantaneous angle of attack through multiplication by α.

Similarly, alternative expressions for C_{m_q} and $C_{m_{\dot\alpha}}$ can be found. Taking the derivative of Equation 16 w.r.t. α and plugging into Equation 3 gives Equation 20.

$$\begin{aligned}
C_{m_q} &= \left(C^T_{L1_\alpha} + c_1 u(\alpha - x_1) + 2c_2(\alpha - x_2)_+ + 3c_3(\alpha - x_3)^2_+ + \ldots\right)\overline{V}^2_T \overline{S}_T \overline{L}^2_T \\
&= C_{m1_q} + C_{m2_q}(\alpha)
\end{aligned} \tag{20}$$

The Macaulay step function $u(\cdot)$ is the derivative with respect to α of the first order spline term in Equation 16. Again two derivatives result. C_{m1_q} is the nominal pitch damping and C_{m2_q} a nonlinear correction term. This term is nonlinear and steady, similar to the parameter in Equation 7. Taking the derivative of Equations 16 and 17 w.r.t. α and plugging into Equation 4 results in one final contribution:

$$\begin{aligned}
C_{m_{\dot\alpha}} = &\left(C^T_{L1_\alpha} + c_1 u(\alpha_t - x_1) + 2c_2(\alpha_t - x_2)_+ + 3c_3(\alpha - x_3)^2_+ + \ldots\right)\cdot \\
&\left(\frac{\partial \varepsilon}{\partial \alpha} + d_1 u(\alpha - y_1) + 2d_2(\alpha - y_2)_+ + 3d_3(\alpha - y_3)^2_+ + \ldots\right)\overline{V}^2_T \overline{S}_T \overline{L}^2_T \\
= &\, C_{m1_{\dot\alpha}} + C_{m2_{\dot\alpha}}(\alpha)
\end{aligned} \tag{21}$$

Again the familiar nominal contribution appears, joined by a nonlinear correction term. At this point, all the familiar aerodynamic parameters have been rewritten as the sum of the linear steady parameters and a corresponding correction term facilitating nonlinear and unsteady aerodynamic modeling. Combining the above gives Equation 22.

$$\begin{aligned}
C_m = &\, C_{m_0} + C_{m1_\alpha}\alpha + C^*_{m1_q} q + C_{m1_{\delta_e}}\delta_e + \\
&+ C_{m2_\alpha}(\alpha(t))\alpha + C_{m2_q}(\alpha) q + C_{m2_{\dot\alpha}}(\alpha)\dot\alpha
\end{aligned} \tag{22}$$

Equation 22 is a new formulation of the pitching moment and a main contribution by this paper. For simplicity it is assumed that the elevator effectiveness $C_{m1_{\delta_e}}$ remains unaffected so that a correction $C_{m2_{\delta_e}}$ is unnecessary. If expressions can be found for C_{m2_α}, C_{m2_q} and $C_{m2_{\dot\alpha}}$ such that they are zero in the linear steady regime, then this model is also valid in the nominal flight regime.

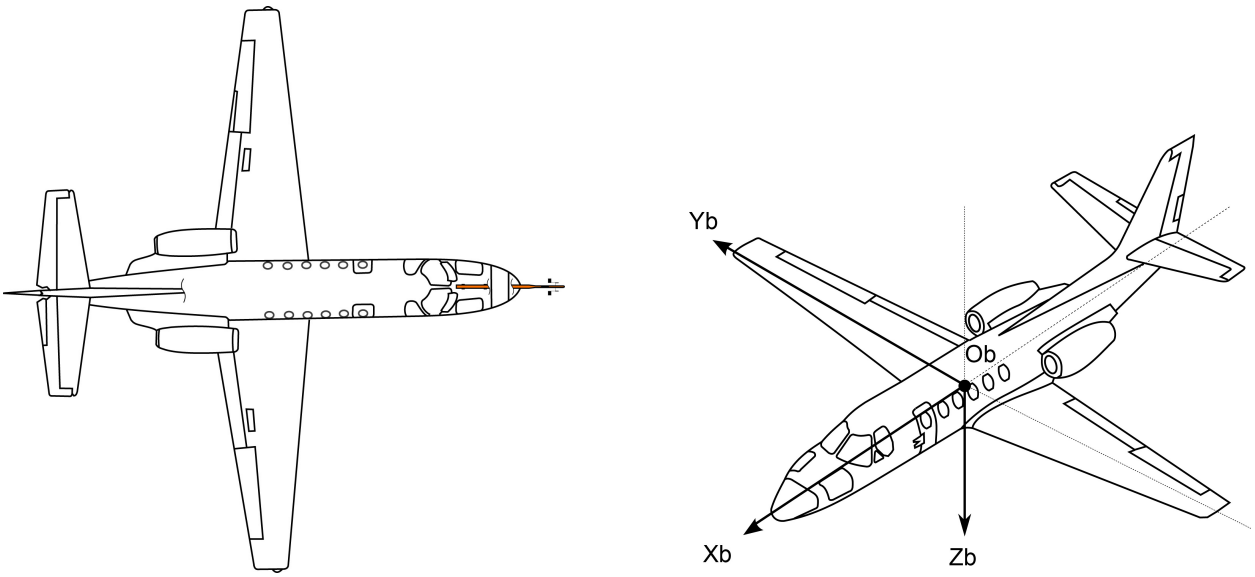

(a) (b)

Fig. 3 Schematic top view (a) and diagonal view (b) of the Cessna Citation II PH-LAB operated by Delft university of Technology and NLR

Table 1 Cessna Citation II PH-LAB Dimensions and mass properties (BEW).

	Parameter	Value
Dimensions	S	30 m^2
	$\overline{b}$	15.9 m
	$\overline{c}$	2.09 m
Mass & Inertia	m	4,157 kg
	I_{xx}	12,392 kg $\cdot$ m^2
	I_{yy}	31,501 kg $\cdot$ m^2
	I_{zz}	41,908 kg $\cdot$ m^2
	I_{xz}	2,252.2 kg $\cdot$ m^2

Table 2 Flight test equipment onboard the Cessna Citation II PH-LAB, and the variables measured relevant for aerodynamic system identification.

Name	Explanation	Measures	Variables	Units
GPS	Global positioning system	Position in F_E	x_e, y_e, z_e	m
		Velocity in F_E	$\dot{x}_e$, $\dot{y}_e$, $\dot{z}_e$	m/s
DADC	Digital air data computer	Total airspeed	V_{TAS}	m/s
AHRS	Attitude and heading reference system	Aircraft attitude	ϕ, θ, ψ	rad
		Body rotation rates	p, q, r	rad/s
		Body specific forces	A_x, A_y, A_z	m/s^2
Synchro	Angle measurements	Control surface deflection	δ_a, δ_e, δ_r	rad
Boom	Air data boom	Air incidence angle	α, β	rad

V. Flight Test Data

The results in this paper are obtained from flight test data only. subsection V.A describes the test aircraft that was used to collect the data, subsection V.B details the specific maneuvers flown for the research, and finally in subsection V.C the data processing procedures and final data set is discussed.

A. Test Aircraft

Flight data was obtained with the Cessna Citation II PH-LAB flying laboratory. This former business jet is operated by the Delft University of Technology and the Netherlands Aerospace Centre (NLR). It has been fully repurposed to serve as a laboratory aircraft. Schematic drawings and an overview of its dimensions and mass properties are shown in Figure 3a and b, and Table 1, respectively. It is equipped with an advanced Flight-Test Instrumentation System (FTIS), that logs the information measured by sensors in flight. These sensors include, amongst others, an air data boom on the nose of the aircraft, that can accurately measure the angle of attack. The available sensors and their measured variables relevant for aircraft system identification are listed in Table 2.

B. Experiment Design

Quasi-random aileron, elevator, and and rudder inputs were used to excite the aircraft over a broad frequency range while in stall. This flight test technique is based on a piloting technique described by Morelli et al. [30]. During the

maneuver, stall is initially entered by reducing airspeed by 1 kts/s until the stall velocity is reached. At this point, the pilots apply disturbances to the control columns, doing this as randomly as possible. Additionally, they apply a bias in order to keep the aircraft in the desired flight condition. In all stalls the elevator was used by one of the two pilots to keep the aircraft in stall. In most stalls, the other pilot would control the ailerons, while in a few cases this would be the rudder or no second actuator at all.

Part of the data set was taken from van Ingen et al., flown in 2018 [12]. These were partly wings-level symmetric stalls, and partly accelerated stalls. In the former, stall is entered in trimmed and level flight. In the latter, stall is entered at a bank angle of 45 degrees, i.e. at 1.4g. The main purpose of the accelerated stalls is do reduce the correlation between pitch rate q and angle of attack rate $\dot{\alpha}$. According to Jategaonkar et al., sufficient decorrelation for system identification is achieved at bank angles over 40 degrees [18]. On the other hand, wings level maneuvers can reach higher angles of attack, and are thus characterized by a deeper stall.

All maneuvers were flown in clean condition, i.e. no flaps and landing gear retracted. Also, the stalls were all flown in a small altitude range around FL170-180. This to not further complicate the data with altitude effects although it is likely that altitude will effect the stall characteristics, as there is a relationship with Mach number [23], and the stall speed is a function of altitude.

C. Flight Data and Pre-Processing

7 accelerated stalls (1.4g) and 11 wings-level stall used by van Ingen et al. [12] were supplemented with 8 additional 1.4g stalls flown in early 2024. This has led to a data set containing 26 stalls, with 15 accelerated stalls and 11 wings-level stalls. All recorded data is pre-processed by means of a zero-phase low-pass Butterworth filter of order 4 and a cut-off frequency of 4 Hz. This ensures that vibrations originating from the stall buffet and noise amplification due to numerical differentiation are removed as much as possible. Modeling of the stall buffet can be done separately as van Horssen et al. showed [31], and is not considered in this paper. Numerical differentiation is required to obtain signals for the angle of attack rate. Furthermore, flight path reconstruction is applied to obtain an improved state estimate. An Unscented Kalman Filter (UKF) was used following up on van Horssen et al. and van Ingen et al. who successfully applied it in their stall modeling efforts [12, 31].

The portion of the flight envelope covered by the maneuvers is visualized in Figure 4 and 5. The data was split in identification and validation data, based on an 80-20 split. The sets 2, 6, 14, 19 and 24 were randomly selected as validation data. Finally, Figure 8 shows the α time traces for an accelerated (stall set 1) and wings-level (stall set 21) stall. There is a clear difference in angle of attack attained. Figure 9 shows the $\dot{\alpha}$ and q time traces in the same sets. In the wings level stall they largely overlap, while in the accelerated stalls they are decorrelated.

The angle of attack time trace in the stall regime appears to be somewhat oscillatory. This is true for each stall in the data set. It is a result of the inherent stability of the aircraft which passively tends to recover from stall. In order to maintain the stall, the pilots have to actively prevent recovery by pulling hard on the control yoke. This leads to a series of stall cycles, where the aircraft oscillates into and out of stall. Throughout the maneuver the stall cycles often tend to become more exaggerated, reaching increasingly higher angle of attack values and rates. Consequently, each maneuver can contain significantly different stall dynamics, such as light and deep stalls.

VI. Methodology

A. System Identification Framework

According to Equation 22 the pitching moment can be split into two parts: one as predicted by the classical linear stability derivative model representing the nominal flight envelope with attached flow, and one that describes the deviation from that flow regime due to stall. The nominal model C_{m1} for the Cessna Citation PH-LAB has been estimated and validated previously by van den Hoek et al. [32]. The parameter estimates can be found in Table 3.

Table 3 Nominal flight envelope parameter estimates by van den Hoek et al. [32].

Parameter	C_{m_0}	C_{m1_α}	$C^*_{m1_q}$	$C_{m1_{\delta_e}}$
Value	0.021	-0.488	-11.9	-1.25

Since this contribution to the pitching moment is already known, there is no need to estimate it in the stall model

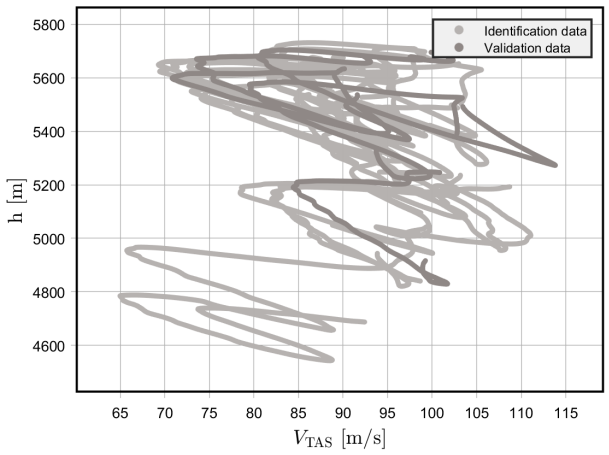

Fig. 4 V_{TAS}-h flight envelope covered by the 26 stall maneuvers.

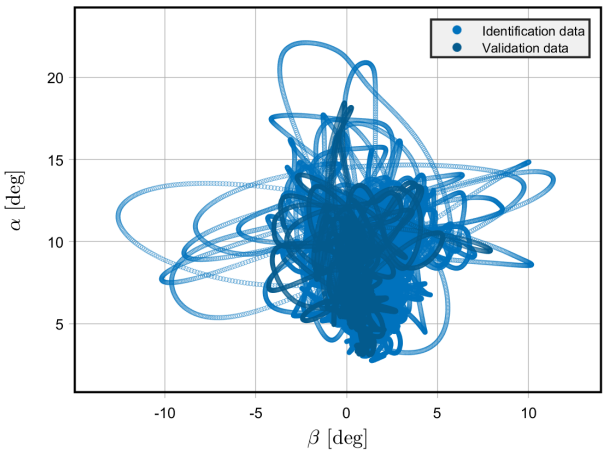

Fig. 5 α-β flight envelope covered by the 26 stall maneuvers.

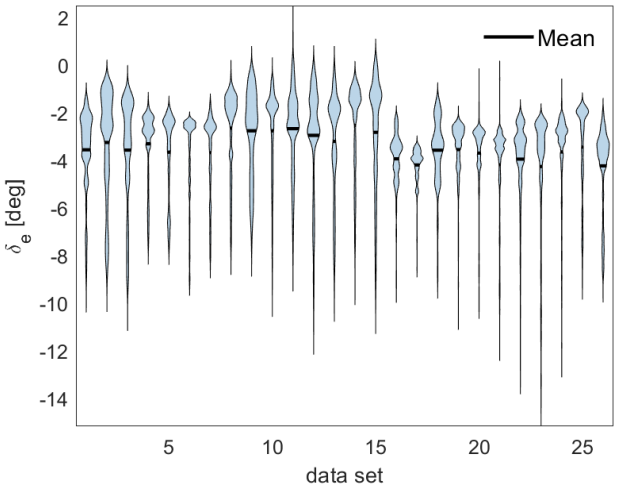

Fig. 6 Violin plots of elevator inputs during the 26 stall maneuvers in the data set.

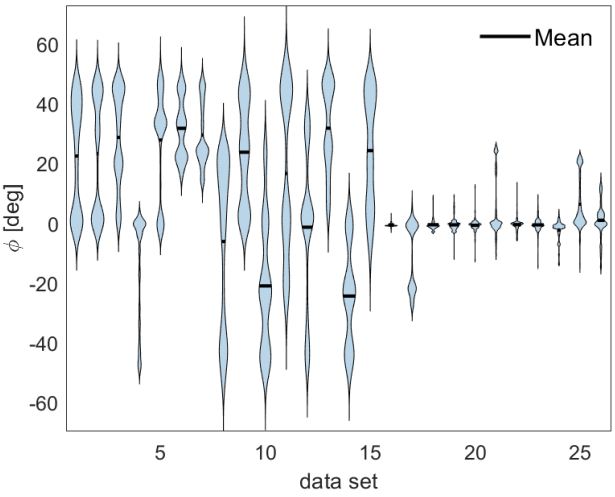

Fig. 7 Violin plots of bank angles during the 26 stall maneuvers in the data set.

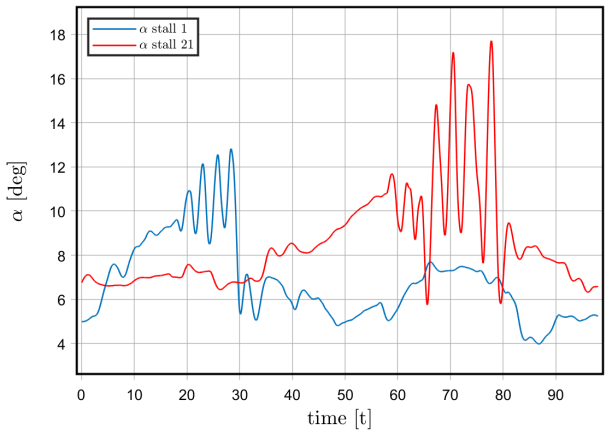

Fig. 8 Time traces of α for an accelerated stall (blue line) and a wings level stall (red line).

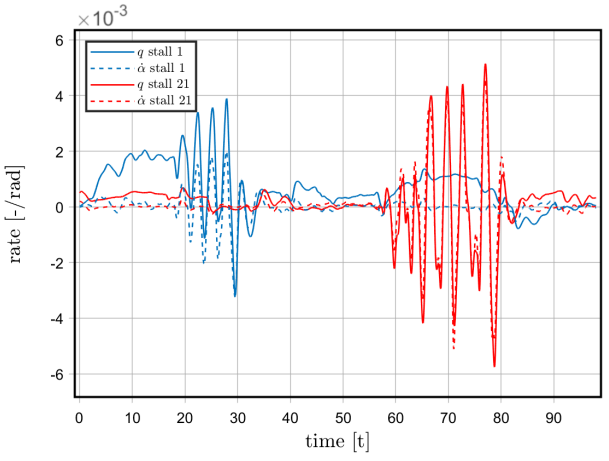

Fig. 9 Time traces of q and $\dot{\alpha}$ for an accelerated stall (blue lines) and a wings level stall (red lines).

identification. Instead, the nominal contribution can be subtracted from the C_m measurements to then identify the stall terms. The nominal model residual is given by Equation 23.

$$
\begin{aligned}
&C_m - C_{m1} = C_{m0} + C_{m_\alpha}(\alpha(t))\alpha + C_{m_q}(\alpha)q + C_{m_{\dot\alpha}}(\alpha)\dot\alpha \\
&\text{where} \\
&C_{m1} = C_{m1_\alpha}\alpha + C^*_{m_q} q + C_{m_{\delta_e}}\delta_e
\end{aligned}
\tag{23}
$$

Note that the bias term C_{m_0} from Table 3 will not be used, as the nominal model bias can simply be recomputed together with the stall bias. This approach essentially provides three free parameters to the stall model.

The next step of the identification framework is to select a set of regressors that can best describe the stall dynamics. Multivariate Orthogonal Function (MOF) modeling will be used to select the stall regressors from a pool of candidates. This pool of candidates will be generated based on Equations 19, 20 and 21. With the model structure known, C_{m2} will be identified using linear regression. Finally, the total pitching moment can then be computed as the sum of the nominal model and the stall model. A flowchart of this system identification framework is provided in Figure 10.

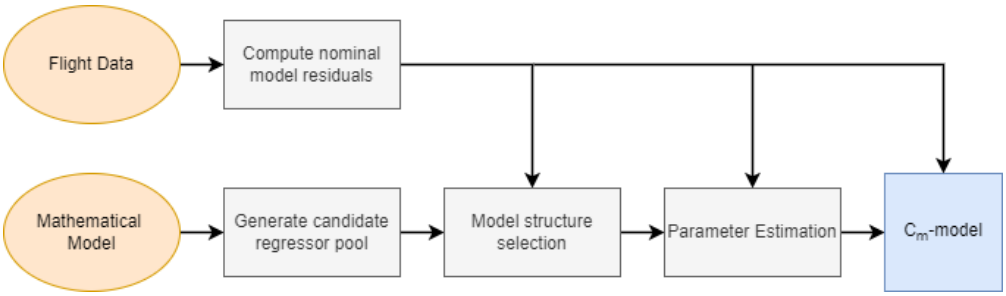

Fig. 10 Flow chart of system identification framework.

B. Candidate Regressor Pool

The mathematical model as formulated in Equation 22 provides some guidance on what terms to include in the model structure. Below the candidate regressors considered for the model are discussed. An overview of all the candidates is given in Table 4

1. α Regressors

$C_{m2_\alpha}(\alpha(t))$ represents a deviation of the pitching moment from from linear steady aerodynamics as predicted by C_{m1_α}. The deviation from linear is a direct result of a simultaneous loss in wing lift and moving COP, and potentially reduced tail lift. The parameter is a function of the time history of α because flow separation and movement of the COP are unsteady. $\alpha(t)$ can be approximated with a Taylor expansion including time derivatives of α up to a certain degree. Alternatively, Morelli shows that lag states of α can also be used as regressors [33]. In the subsequent α_{t-k} denotes such a lag state, where k is the lag. With a sampling frequency of 100 Hz, α_{t-k} represents the α measurement $\frac{k}{100}$ s prior to time t. To increase model complexity, higher order and cross terms of the lag states can be included in the model. It was decided to include a time lag up to 0.3 s, represented by α_{t-30}. Such a wide range of lags can be included because the MOF algorithm will be used to select a small subset of the candidates. The only drawback of many candidates is some additional computation time.

C_{m2_α} was derived as the derivative of C_{m2} with respect to α_t, therefore the total moment contribution for the α regressors is obtained by multiplying with α_t. Regressors up to third order are included in the candidate pool.

2. q Regressors

$C_{m2_q}(\alpha)$ represents changes in the pitch damping due to a potentially nonlinear tail lift at high α. The contribution to C_{m2_q} by the wing is neglected. This can be justified by the very small moment arm of the wing lift compared to that of the tail. Equation 20 provides inspiration for good candidate regressors. It includes spline basis functions with zero order continuity (i.e. continuous, but not differentiable at the knots). The point where the splines become active is

unknown; if this point lies within the stall envelope at all, a large range of spline knots is included in the candidate pools. It was decided to choose a range between 0 and 20 deg. Examples of these spline terms are provided in Table 4.

3. $\dot{\alpha}$ Regressors

$C_{m2_{\dot{\alpha}}}(\alpha)$ represents changes in the downwash lag damping due to a combined nonlinear tail lift and downwash gradient at high α. Similar to C_{m2_q}, spline terms are used to model it. In this case however, the regressors can be a multiplication of two splines with different knots, as suggested by Equation 21.

4. Other Regressors

Finally, three more candidates are included in the candidate pool. First of all there is a bias. Secondly, the elevator deflection is included to compensate for any potential model errors in the model by van den Hoek et al.. Lastly, the thrust coefficient C_T is part of the pool. This model term was found to be beneficial for model quality by van Ingen et al. [12]. Since the current data set is largely the same, it is likely that C_T will again positively contribute. Appendix C from the aforementioned paper by van Ingen et al. is referred to for an explanation on the inclusion of C_T.

Table 4 Candidate Regressors Pitching Moment Model (100Hz sampling frequency)

Order	Regressor	Order	Regressor
$\underline{C_m - \alpha}$		$\underline{C_m - \dot{\alpha}}$	
1	α_t	0	$u(\alpha-0°)\dot{\alpha}, u(\alpha-1°)\dot{\alpha}, \dots, u(\alpha-20°)\dot{\alpha}$
2	$\alpha_t^2, \alpha_{t-1}\alpha_t, \alpha_{t-2}\alpha_t, \dots, \alpha_{t-30}\alpha_t$	1	$u(\alpha-0°)(\alpha-0°)_+\dot{\alpha}, u(\alpha-0°)(\alpha-1°)_+\dot{\alpha}, \dots,$ $u(\alpha-11°)(\alpha-14°)_+\dot{\alpha}, \dots, u(\alpha-20°)(\alpha-20°)_+\dot{\alpha}$
3	$\alpha_t^3, \alpha_{t-1}\alpha_t^2, \dots, \alpha_{t-18}\alpha_{t-24}\alpha_t, \dots, \alpha_{t-30}^2\alpha_t$	2	$(\alpha-0°)_+^2\dot{\alpha}, (\alpha-0°)_+(\alpha-1°)_+\dot{\alpha}, \dots,$ $(\alpha-9°)_+(\alpha-17°)_+\dot{\alpha}, \dots, (\alpha-20°)_+^2\dot{\alpha}$
$\underline{C_m - q}$			
0	$u(\alpha-0°)q, u(\alpha-1°)q, \dots, u(\alpha-20°)q$	*other*	
1	$(\alpha-0°)_+q, (\alpha-1°)_+q, \dots, (\alpha-20°)_+q$		$1, \delta_e, C_T$
2	$(\alpha-0°)_+^2q, (\alpha-1°)_+^2q, \dots, (\alpha-20°)_+^2q$		

C. Model Structure and Parameter Estimation

Table 4 provides a finite set of candidate regressors for the stall model, however the question remains what subset yields the optimal model. Many of the candidates do not represent the real underlying physics that generated the data, and should therefore not be part of the model structure. Furthermore, a good model will include enough model terms to capture the complex stall dynamics but not overfit the data. However, the chosen model complexity must be justified by the information content in the data. If that is not the case, the model will overfit the identification data and not generalize well to unseen data. Another challenge is preventing highly correlated regressors. Including such variables in the model structure will also inevitably lead to overfitting and large parameter variances. These considerations are especially important in this problem, due to the size and the potential correlations between the entries of the candidate regressor pool.

1. Multivariate Orthogonal Function Modeling

Morelli developed a combined model structure selection and parameter estimation techniques for nonlinear aerodynamic modeling [20, 21]. This technique uses empirical multivariate orthogonal functions. Originally, it was applied in a quasi-steady context, i.e. using the instantaneous values of the candidate regressors [30]. Later, Morelli also deployed the same method to identify unsteady model terms, including lag states of α [33]. The MOF method picks model terms from a pool of candidates in an iterative fashion. On each step of the algorithm, all candidate regressors are assessed based on their potentially beneficial contribution to reducing a cost function. Then after every iteration the best candidate is added to the model structure until the cost function is minimized. The cost function penalizes both model error and model complexity. The candidate regressors are always orthogonalized with respect to the regressors in

the model structure to avoid correlated entries.

In the subsequent, regressors in physical coordinates will be referred to by $\mathbf{x}_i$, whereas orthogonalized regressors will be referred to as $\mathbf{p}_i$. At initialization, a bias term is included in the model structure:

$$\mathbf{x}_1 = \mathbf{p}_1 = \mathbf{1} \tag{24}$$

At this point and after every iteration of the algorithm, a Gram-Schmidt orthogonalization procedure is applied to all remaining candidate regressors yielding $\mathbf{p}_j$:

$$\begin{aligned} &\mathbf{p}_j = \mathbf{x}_j - \sum_{k=1}^{j-1} \gamma_{k,j} \mathbf{p}_k, \quad j = 2, 3, \ldots, n \\ &\text{where:} \\ &\gamma_{k,j} = \frac{\mathbf{p}_k^\intercal \mathbf{x}_j}{\mathbf{p}_k^\intercal \mathbf{p}_k} \end{aligned} \tag{25}$$

All orthogonalized candidates are individually assessed based on the improvement that the inclusion of the candidate yields to the predicted square error (PSE) metric. The PSE constitutes two parts; one ensuring a close fit to the data through an MSE term, and a regularization term that penalizes model complexity. The best candidate is added to the model structure. The PSE metric is given in Equation 26, and the individual contribution by the jth candidate is given in Equation 27.

$$\text{PSE} = \frac{(\mathbf{y} - \hat{\mathbf{y}})^\intercal (\mathbf{y} - \hat{\mathbf{y}})}{N} + \sigma_y^2 \frac{n}{N} \tag{26}$$

$$\Delta\text{PSE}_j = -\frac{(\mathbf{p}_j^\intercal \mathbf{y})^2}{\mathbf{p}_j^\intercal \mathbf{p}_j} + \sigma_{\max}^2 \frac{1}{N} \tag{27}$$

$\hat{\mathbf{y}}$ is the model output using the model structure at the current iteration, and $\mathbf{y}$ the measurement vector, in this case always C_m. N is the number of data points, n the number of terms already included in the model and σ_{max}^2 is the upper bound variance of $\mathbf{y}$. The upper bound was taken as $\sigma_{\max}^2 = 25 \cdot \sigma_y^2$. The candidate providing the largest reduction in PSE is selected and added to the model structure. Subsequently, the algorithm is repeated until $\Delta\text{PSE}_j \geq 0$ for all j. Namely, if that condition is satisfied, there are no more candidates that justify an increased model complexity by their contribution to the model fit. The set of orthogonal vectors is now collected in matrix $\mathbf{P} = \left[\mathbf{p}_1 \mathbf{p}_2 \ldots \mathbf{p}_n\right]$. Using ordinary least squares, a set of parameters $\hat{\boldsymbol{\phi}}$ that minimize the MSE (not the PSE) can be found.

$\hat{\boldsymbol{\phi}}$ is associated with the orthogonalized regressors in $\boldsymbol{P}$. Both can be easily transformed to physical space using Equation 28 and Equation 29, where the transformation matrix $\boldsymbol{\Gamma}$ is given by Equation 30.

$$\hat{\boldsymbol{\theta}} = \boldsymbol{\Gamma}^{-1} \hat{\boldsymbol{\phi}} \tag{28}$$

$$\boldsymbol{X} = \boldsymbol{P}\boldsymbol{\Gamma} \tag{29}$$

$$\boldsymbol{\Gamma} = \begin{bmatrix} 1 & \gamma_{1,2} & \gamma_{1,3} & \cdots & \gamma_{1,n} \\ 0 & 1 & \gamma_{2,3} & \cdots & \gamma_{2,n} \\ 0 & 0 & 1 & \cdots & \gamma_{3,n} \\ \vdots & \vdots & \vdots & \ddots & \vdots \\ 0 & 0 & 0 & 0 & 1 \end{bmatrix} \tag{30}$$

Then the model output is computed as:

$$\hat{\boldsymbol{y}} = \boldsymbol{X}\hat{\boldsymbol{\theta}} = \boldsymbol{P}\hat{\boldsymbol{\phi}} \tag{31}$$

Due to the iterative procedure, some of the model terms added early on in the process might end up negatively contributing to the MSE. Therefore, after the model structure is finalized, it is checked for each regressor how the MSE

changes if it is excluded. If the reduction in Root Mean Square (RMS) of the model output falls below a threshold of 0.5%, the term is removed, with the RMS calculated by Equation 32.

$$\text{RMS} = \frac{1}{N}\sqrt{\hat{\mathbf{y}}^\intercal \hat{\mathbf{y}}} \tag{32}$$

2. Practical Considerations

The MOF algorithm is applied in two stages. Firstly, only the first two rows of the α, q and $\dot{\alpha}$ candidates from Table 4 are included in the candidate pool. Then the model terms picked in the first stage are frozen into the model structure. Now on the second stage the highest order regressors are tested. If any of them can still provide a positive contribution to the PSE, they are included as well. Applied in this way, potential overfitting issues can be prevented.

Furthermore, all identification data consisting of multiple stalls is combined into a single large dataset as input to the MOF algorithm, as opposed to the approach of using each stall individually, as was done in earlier stall modeling efforts (e.g. van Ingen et al. [12]) have done.

D. Validation Approach

Stall dynamics are very complex and each stall may vary in several (unobservable) aspects. Consequently it can be difficult to determine the accuracy of the model by assessing only the validation data. Each stall set consists of a series of cycles as discussed in subsection V.C. The cycles all have one thing in common, i.e. the angle of attack time trace starts at some minimum, reaches a maximum, to end with another minimum. This way the aircraft oscillates in and out of the stall regime. The angle of attack can be approximated as a cosine with some mean α_0 in rad, amplitude α_1 in rad and radial frequency ω in rad/s:

$$\alpha(t) = \alpha_0 + \alpha_1 \cos \omega t \tag{33}$$

The model will be evaluated against an array of such cosine functions, with different amplitudes and frequencies.

To assess the model performance on real flight data, individual stall sets will be looked at. A comparison is made to the model by van Ingen et al. [12]. The model structure that was found by van Ingen for the pitching moment is given by Equation 34.

$$C_m = C_{m_0} + C_{m_\alpha}\alpha + C_{m_{\delta_e X}} \max\left(\frac{1}{2}, X\right)\delta_e + C_{m_{C_T}} C_T \tag{34}$$

Here X represents the point of flow separation on the wing. It is an internal state and requires a nonlinear model optimization as described by van Ingen et al. and others [12, 13, 31].

VII. Results

A. Dynamic Stall Phenomena in Flight Test Data

Some of the dynamic stall effects that have been observed in wind tunnel tests with airfoils are also present in the flight test data collected for this paper. The lift and moment hysteresis for a stall cycle in the first stall set is shown in Figure 11. This stall is classified as a light stall because the counterclockwise loop at the end of the upstroke of the moment curve is missing. The plateau and subsequent vortex lift can be clearly recognized, indicating the formation and shedding of the DSV. Thereafter, the lift stall is very abrupt. Furthermore, the moment stall has been indicated as the first point where C_m decreases. The lift and moment stall occur at samples 134 and 147 of this data segment, respectively. With a sampling frequency of 100 Hz, the lag between the two events is 0.13 s.

In most deep stall cycles the lift plateau is not visible, although it is in some. Also the lift and moment stalls are much less abrupt. Figure 12 illustrates this. Note the small loop in the bottom right of the moment hysteresis, indicating deep stall. This stall only slightly enters the deep stall regime, yet the stall behavior is completely different compared to that of the light stall. Here, the moment stall again precedes the lift stall. The moment stall indicates the point where the slope of the moment curve changes to a more negative slope. This point can be found easily as a negative peak in the second (numerical) time derivative of C_m. In this case the two events occur 0.17 s apart.

Figure 11 and Figure 12 are two stall cycles taken from accelerated stall maneuvers. Due to the large bank angle these maneuvers cannot reach a large angle of attack. The wings-level stalls can reach angle of attack > 20 degrees,

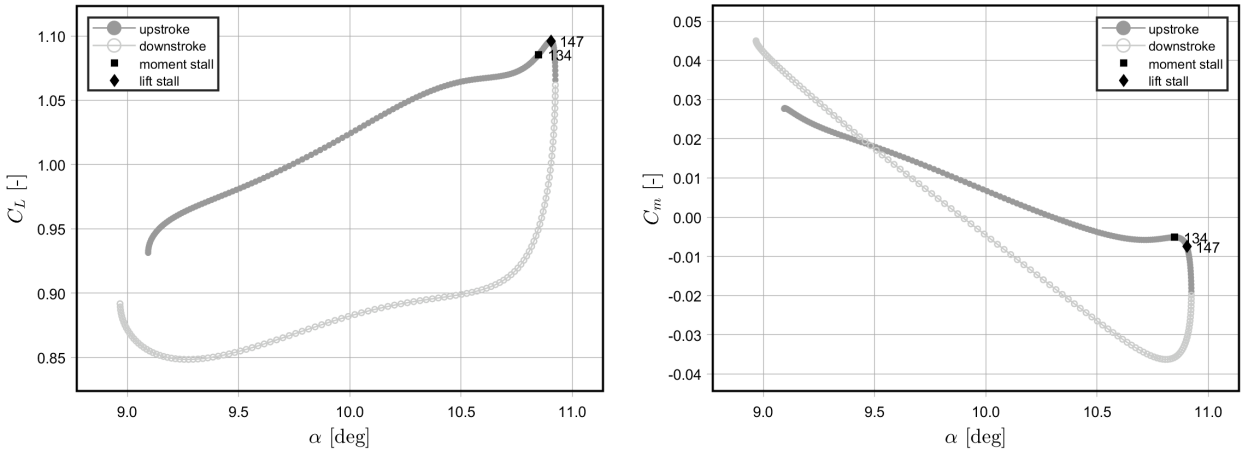

Fig. 11 Lift (left) and moment (right) hysteresis for a light stall with the PH-LAB in stall set 1.

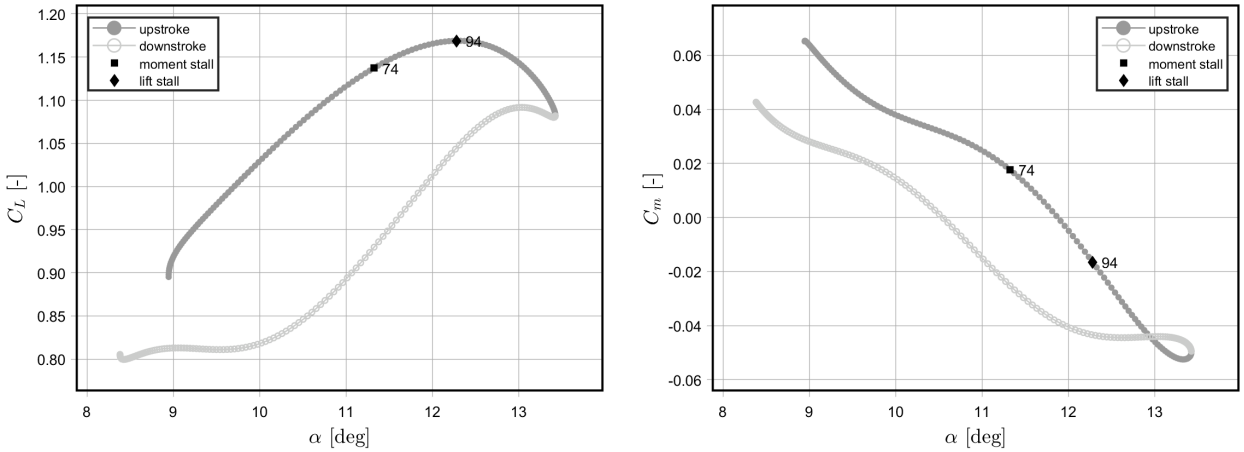

Fig. 12 Lift (left) and moment (right) hysteresis for a stall with the PH-LAB just penetrating the deep stall regime in stall set 2.

which for the PH-LAB should be considered a deep stall; Figure 13 shows one of the most severe stalls in the data set. Whereas the size of counterclockwise deep stall loops typically appears to increase with increasing angle of attack, it completely disappears for these deepest stalls. Again the lift stall, and the moment stall as defined for deep stall previously, are indicated. The lift and deep stall are now 0.63 s apart. This lag does not relate logically to moment stall caused by the DSV. Instead the moment stall in the deep stall might be a nonlinearity in the pitching moment, occurring at around 12 deg angle of attack. Yet, there is the appearance of a small plateau in the lift hysteresis. It seems that vortex formation continues to occur at higher angles of attack, but having a smaller impact. This also explains the lesser degree of abruptness in the lift and moment stalls.

B. Pitching Moment Model

The first iteration of the MOF algorithm yields the model structure in Equation 35. This model was selected from the candidate pool in Table 4, excluding the highest order regressors for each α, q and $\dot{\alpha}$. On the second iteration the highest order regressors where included but no additional model terms were selected.

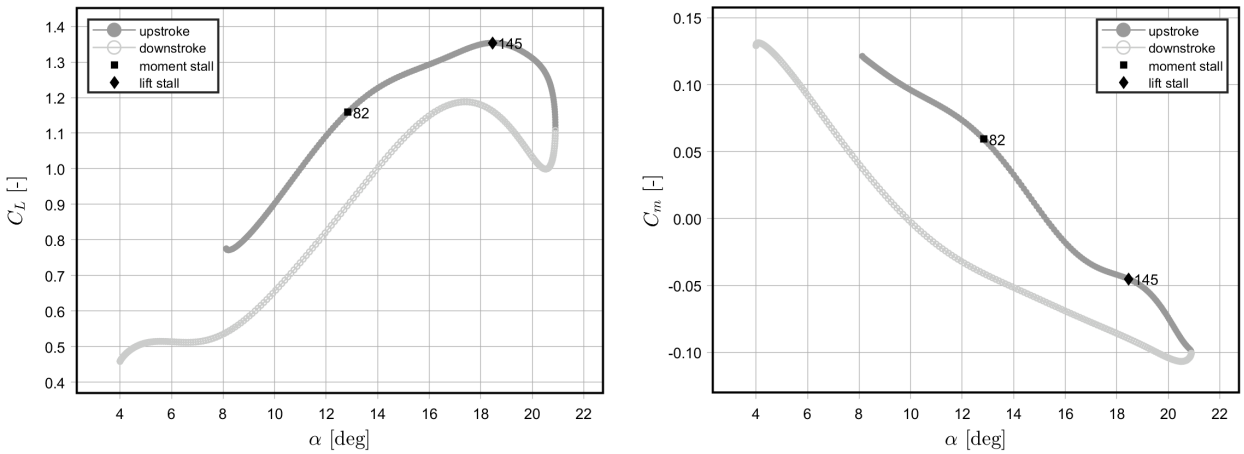

Fig. 13 Lift (left) and moment (right) hysteresis for a deep stall with the PH-LAB in stall set 22.

$$
\begin{aligned}
C_m &= C_{m0} + C_{m1_\alpha}\alpha + C^*_{m1_q} q + C_{m1_{\delta_e}}\delta_e \\
&\quad + C_{m2_\alpha}\alpha + C_{m2_q} u(\alpha_t - 5^\circ) q + C_{m2_{\dot\alpha}} u(\alpha_t - 8^\circ)\dot\alpha + C_{m2_{\delta_e}}\delta_e + C_{m2_{C_T}} C_T \\
&\text{where} \\
C_{m2_\alpha} &= C_{m2_{\alpha_t}} + C_{m2_{\alpha_t^2}}\alpha_t + C_{m2_{\alpha_{t-7}\alpha_t}}\alpha_{t-7} + C_{m2_{\alpha_{t-30}\alpha_t}}\alpha_{t-30}
\end{aligned}
\tag{35}
$$

It can be seen that C_{m2_α} consists of four model terms, and three different states of α. Furthermore, a correction on $C^*_{m1_q} q$ is activated starting at an angle of attack of five degrees and a dependency on $\dot\alpha$ is introduced for angles of attack larger than eight degrees. Finally, an additional elevator term is selected, and a thrust coefficient term. Parameter estimates and the corresponding parameter standard deviations are provided in Table 5.

Table 5 Stall model parameter estimates and corresponding parameter standard deviations.

Parameter	C_{m0}	$C_{m2_{\alpha_t}}$	$C_{m2_{\alpha_t^2}}$	$C_{m2_{\alpha_{t-7}\alpha_t}}$	$C_{m2_{\alpha_{t-30}\alpha_t}}$	C_{m2_q}	$C_{m2_{\dot\alpha}}$	$C_{m2_{\delta_e}}$	$C_{m2_{C_T}}$
Estimate	0.0145	0.271	93.4	-125	32.0	11.5	4.83	0.965	0.182
Standard Error	0.0216	0.297	35.9	42.7	8.66	3.57	9.92	0.153	0.0508

The correlation matrix of the stall model regressors is given in Table 6. The correlations between the various α states are significant. the cross correlations between each of them are practically unity, as is to be expected. The selection of all these regressors underlines the richness of the information content in the data. Despite these high correlations, 4 model terms could be selected without excessive parameter standard deviations. Furthermore, the correlation between the q and $\dot\alpha$ splines shows the benefit of the spline terms. Over all the identification data, the correlation between q and $\dot\alpha$ is 0.825, whereas between $u(\alpha - 5^\circ)q$ and $u(\alpha - 8^\circ)\dot\alpha$ it is only 0.729.

C. Aerodynamic Parameters

1. C_{m_α}

As C_{m2_α} is a function of multiple lag states, it is in essence a combined α and α-time derivative parameter. In fact, this parameter includes information on the first and second α time derivatives, because it includes three different α states. In other words, it could also be written as $C_{m2_\alpha}(\alpha, \dot\alpha, \ddot\alpha)$.

In the steady state, C_{m2_α} reduces to a pure α parameter. Once the angle of attack is no longer subject to change, the transient washes out in at most 0.3 s, which with a sampling frequency of 100Hz implies 30 time steps. After 0.07

Table 6 Stall model regressor correlation matrix.

	Variable	1	2	3	4	5	6	7	8
1	α_t	1							
2	α_t^2	0.974	1						
3	$\alpha_{t-7}\alpha_t$	0.973	0.999	1					
4	$\alpha_{t-30}\alpha_t$	0.968	0.991	0.994	1				
5	$u(\alpha-5°)q$	0.169	0.139	0.114	0.037	1			
6	$u(\alpha-8°)\dot{\alpha}$	-0.004	-0.005	-0.035	-0.126	0.729	1		
7	δ_e	-0.418	-0.399	-0.399	-0.401	-0.129	-0.000	1	
8	C_T	-0.826	-0.784	-0.782	-0.780	-0.178	-0.074	0.358	1

s (7 time steps at 100Hz) the second derivative information disappears, since now α_{t-7} equals α_t, and thus only two different α values are known. After 0.3 s, α_{t-30} will be equal to α_t and C_{m2_α} is merely a function of the instantaneous angle of attack. Similarly, in slow motions where unsteady phenomena are not to be expected, the same logic holds up. The three α states will then also be approximately equal.

$$C_{m2_\alpha}\alpha = -0.0333\alpha^2 + 0.271\alpha \tag{36}$$

Equation 36 represents the moment contribution for a constant α. The parameter estimates for $C_{m2_{\alpha_t^2}}$, $C_{m2_{\alpha_{t-7}\alpha_t}}$ and $C_{m2_{\alpha_{t-30}\alpha_t}}$ approximately add up to 0, resulting in a constant steady state C_{m2_α}. Figure 14 shows this relationship.

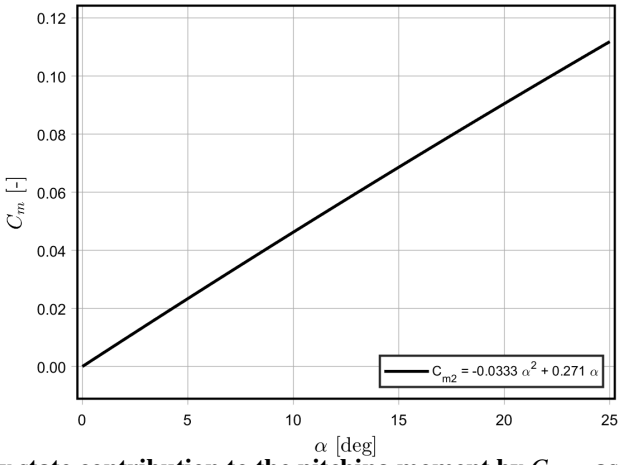

Fig. 14 Steady state contribution to the pitching moment by C_{m2_α} as a function of α.

C_{m2_α} was intended to represent the stall dynamics' deviation from the moment generated by the nominal wing and tail lift. The positive value in the steady state can be explained by a reduced wing and tail lift, increasing the negative pitching moment around the CG.

In order to gain insight in the unsteady modeling capacity of C_{m2_α}, the response to cosine signals with various frequencies is analyzed. Figure 15 shows five low amplitude oscillations (α_0=10° and α_1=2.5°) with various frequencies. These low amplitude oscillations are a typical representation of the α range in a 1.4g accelerated stall. The middle and lower plot show C_{m2_α} and its contribution to C_m for one period of each oscillation, respectively. This indicates that each point on the x-axis represents the same angle of attack for all curves. Yet, the corresponding pitching moment values differ across the curves, highlighting the influence of the motion prehistory. The slowest signal approximates a constant C_{m2_α}, making it a steady motion since there is no dependency on time. Furthermore, it can be seen that there is a relationship between the frequency and the peak value of the negative moment. This is the same relationship that is mentioned in the works of the likes of McCroskey and Carr [14, 22].

Figure 16 shows the exact same relationships but for a large amplitude oscillation with a higher mean (α_0=15° and α_1=5°), that is more representative of a wings-level stall. The relationship between the negative moment peak and the

oscillation frequency is also here clear. The major difference is the magnitude of the peaks. The peaks in the large amplitude oscillations reach values four times higher than the low amplitude oscillations.

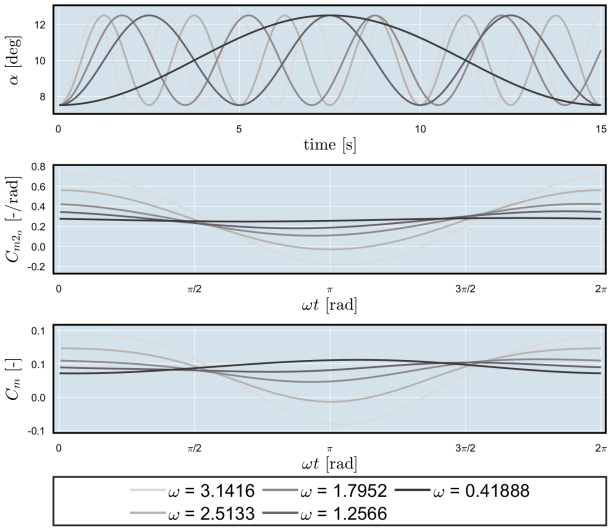

Fig. 15 Signal $\alpha = 10 - 2.5\cos\omega t$ for 5 frequencies (top) and corresponding C_{m2_α} (middle) and C_m (bottom) throughout the stall cycle.

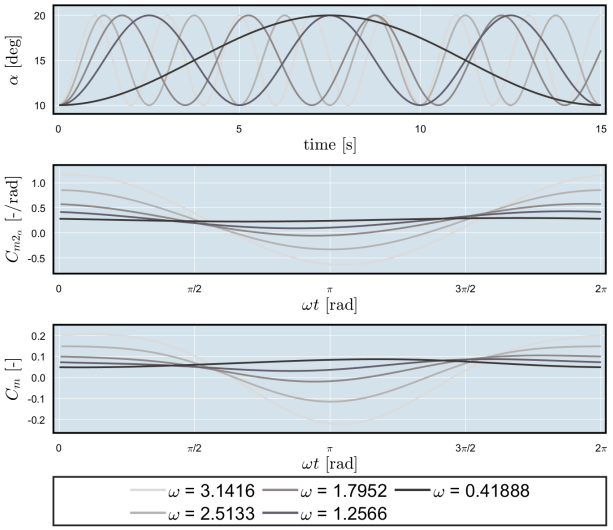

Fig. 16 Signal $\alpha = 15 - 5\cos\omega t$ for 5 frequencies (top) and corresponding C_{m2_α} (middle) and C_m (bottom) throughout the stall cycle.

Figure 17 show the contributions to the pitching moment plotted against α as modeled by C_{m2_α} for the high amplitude motion from Figure 16, but only for the three highest frequencies. An interesting pattern emerges. As seen before, the contribution to C_{m2} from the slower motions is not significant. However, the left hysteresis curve in Figure 17 reveals that this slower motion contributes to a counter clockwise hysteresis loop, associated with stable damping. On the other hand, the slightly faster motion in the middle of Figure 17 exhibits no hysteresis. Finally, the fastest motion in the right curve of Figure 17 is characterized by a loop reversal, i.e. the hysteresis is now clockwise. The offset in moment can be explained by different wing lift force and moment arm during the up- and downstroke. The tail lift is assumed independent of the prehistory of the angle of attack, and therefore no different during up- and downstroke. With only the moment curves, it is difficult to say what phenomenon exactly causes the loop reversal. A model for the lift hysteresis could be insightful since it would exclude the effects of the moving center of pressure.

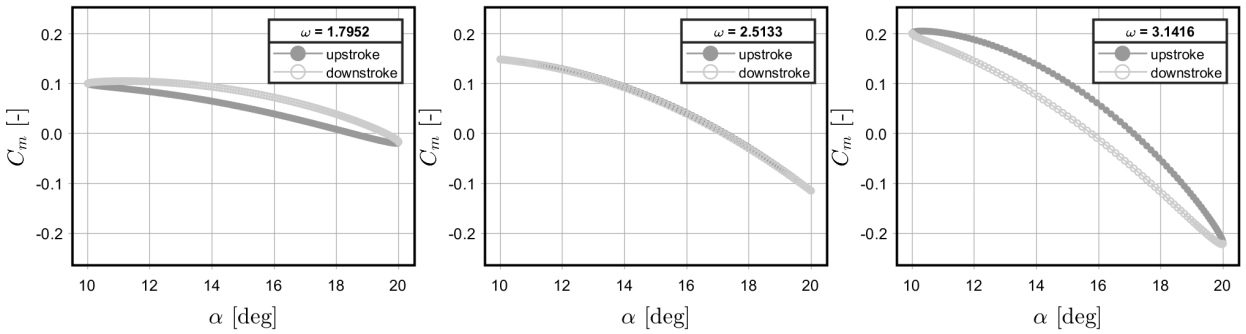

Fig. 17 Moment hysteresis as modeled by C_{m2_α} for signal $\alpha = 15 - 5\cos\omega t$ with frequencies from left to right: $\omega = 1.7952$, $\omega = 2.5133$ and $\omega = 3.1416$.

2. C_{m_q} and $C_{m_{\dot\alpha}}$

As indicated in Equation 35 both an additional pitch rate as well as an angle of attack rate parameter were selected in the model structure selection process. The stall induced pitch damping is modeled by C_{m2_q} as a spline of degree 0 in

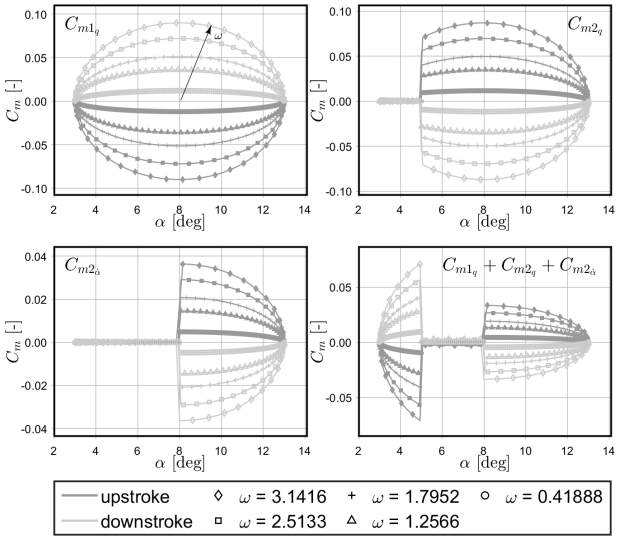

Fig. 18 Moment hysteresis as modeled by the three aerodynamic rate derivatives for signal $\alpha = 8 - 5cos(\omega t)$ with 5 frequencies.

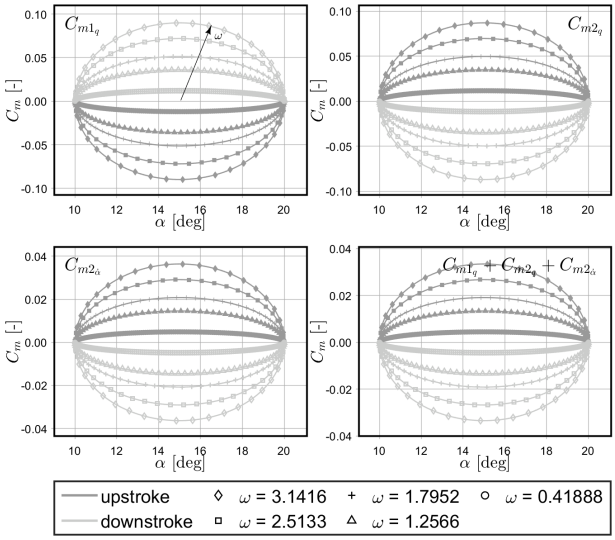

Fig. 19 Moment hysteresis as modeled by the three aerodynamic rate derivatives for signal $\alpha = 15 - 5cos(\omega t)$ with 5 frequencies.

α, so that an additional constant contribution is introduced at angle of attack larger than 5°. C_{m2_q} practically cancels the nominal pitch damping C_{m1_q}: The nominal value stands at -11.9 and the stall parameter increases it by 11.5 to -0.4. With the pitch damping defined as given by Equation 3, this result implies that the tail lift slope becomes zero at angles of attack above 5°. It is not very probable that this is indeed the case because this point falls well within the attached flow regime. It should be noted that this result is only a low order approximation and it is likely that more and higher order pitch damping terms are needed to capture the exact relationship. However, given the information content of the data, this is not realistic.

A similar zero order spline term is selected for the downwash lag coefficient $C_{m2_{\dot{\alpha}}}$. With a value of 4.83 the total damping from the rate derivatives is taking a positive, and thus aerodynamically unstable, value at angles of attack above 8°. Given Equation 4 and the earlier observed pitch damping, this result suggests a decreased downwash gradient.

Despite the introduction of spline terms, q and $\dot{\alpha}$ are significantly correlated (see Table 6). Additionally, the combined α derivatives also hold information about the angle of attack rate. It is therefore plausible that some of the contributions are exchanged between the various model terms.

Similar to subsubsection VII.C.1, some artificial cosine signals are used to investigate the rate contributions. The derivative of the standard cosine signal from Equation 33 is normalized by $\frac{\bar{c}}{V_{\text{stall}}}$ with $V_{\text{stall}} \simeq 75$ m/s to obtain a unitless $\dot{\alpha}$. Figure 18 shows hysteresis plots of oscillations that cover both the C_{m2_q} and $C_{m2_{\dot{\alpha}}}$ knots. The contributions from the nominal and 2 stall contributions are shown. In the bottom right the combined effect is shown. The advantage of this model is that once the angle of attack falls below 5° the exact same damping characteristics are restored as in the nominal model. It can be seen that higher frequency motions have a larger swept out area, as is to be expected.

Figure 19 shows the same hysteresis plots for a signal with a higher mean at $\alpha_0 = 10°$. This is a good representation of a deeper stall. It shows that these stall completely operate in the regime with the unstable aerodynamic damping.

The dependency in Figure 18 and 19 on the motion frequency is straightforward. These derivatives only describe a quasi-steady contribution to the pitching moment. Therefore it makes sense that there are no surprising frequency dependent effects. These terms model the volume in the moment hysteresis, while C_{m2_α} can capture more intricate time dependent relationships.

D. Hysteresis Modeling

The motions considered in subsection VII.C are artificial and idealized. In the subsequent, the modeling capacity of the α and rate derivatives is analyzed for actual flight test data, to see how the model handles the hysteresis observed in the pitching moment.

Figure 20 shows the contributions by the α related model parameters for the modeling of the stall cycle in Figure 12

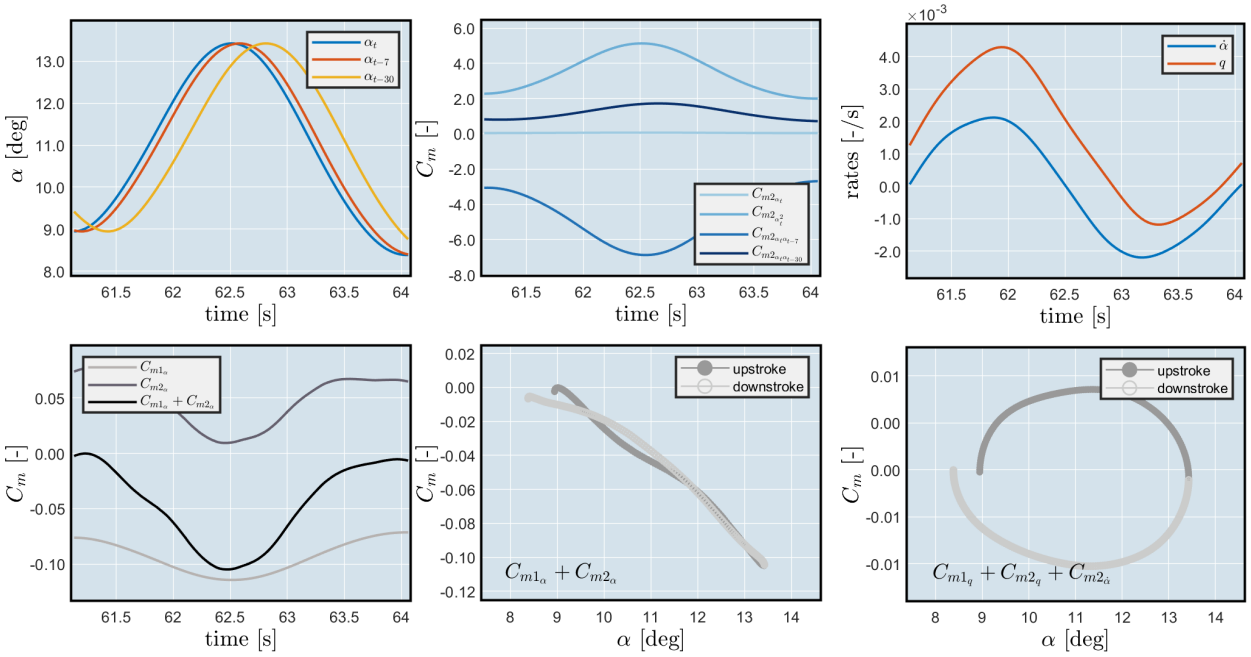

Fig. 20
Contribution to the pitching moment by by α for the deep stall in Figure 12.

Fig. 21 Contribution to the pitching moment by by q and $\dot\alpha$ for the deep stall in Figure 12.

discussed previously. In the top row, the various lag states of α are shown, as well as their individual contributions to the pitching moment. $C_{m_{\alpha_t}}$ has a small contribution in the stall. This parameter mainly provides a correction on the steady state behavior, where the other three contributions add up to approximately zero (see subsubsection VII.C.1). $C_{m_{\alpha_t^2}}$, $C_{m_{\alpha_{t-7}\alpha_t}}$ and $C_{m_{\alpha_{t-30}\alpha_t}}$ have large contributions that individually lack real physical interpretation. However, jointly they can capture subtle changes in the pitching moment. Compare the moment hysteresis curve in Figure 12 to the one in Figure 20 and note how subtle changes in the slope of the pitching moment are modeled. Barely any hysteresis is modeled by C_{m2_α}. That contribution is provided by q and $\dot\alpha$, as shown in Figure 21.

Figure 22 is an even better display of the collaborative effort provided by $C_{m_{\alpha_t^2}}$, $C_{m_{\alpha_{t-7}\alpha_t}}$ and $C_{m_{\alpha_{t-30}\alpha_t}}$. It shows the stall model contributions for the modeling of the data in Figure 13. Whereas the α contributions in Figure 20 joined to form a single negative peak, in Figure 22 three small peaks form. The α regressors also model various hysteresis loops: a small and large counter clockwise, and a small clockwise one. Again the volume in the moment hysteresis is captured by the rate derivatives as shown in Figure 23.

E. Model Validation

The model presented in the form of Equation 35 provides an alternative to the Kirchhoff based method. To assess its predictive capabilities the MSE of the C_m predictions resulting from this model and the one by van Ingen et al. [12] are compared. Table 7 displays the model performances in terms of MSE for both identification and validation data.

Clearly, the model presented in this paper is superior in terms of minimization of the MSE. It provides an improvement of 64.3% over all identification data, while over all validation data an improvement of 55.9% can be reported. It is important to note that a large part of the performance improvement is due to the modeling performance outside the stalls. Every stall set includes a significant portion of data pre- and post-stall. The top plot in Figure 24 shows an example. These are the time traces of C_m of validation stall 14. Especially in the post stall, the model is much closer to the measurements. In the isolated stall cycles, it outperforms the model by van Ingen et al. as well, although the difference is less striking in the wings-level stalls.

The bottom plot in Figure 24 reveals a model deficiency in both models, although much more severe in the model by van Ingen et al.. This shows the same data as the top plot, but zoomed in on the stall cycles. The model predictions are

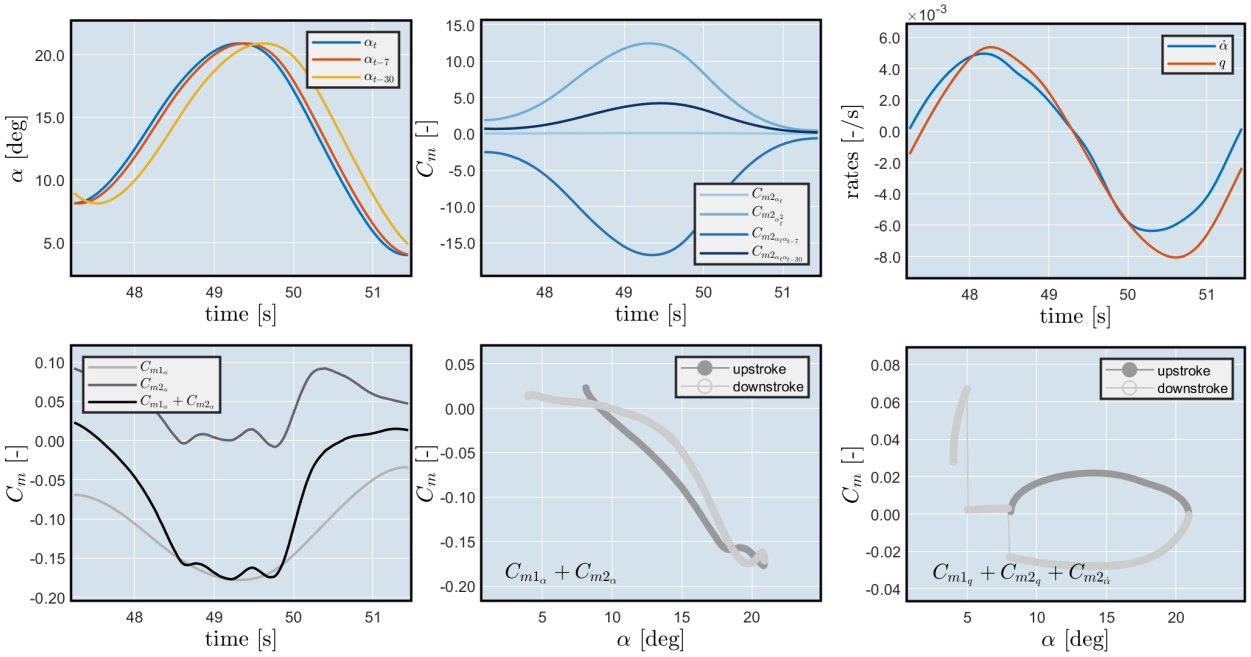

Fig. 22
Contribution to the pitching moment by by α for the deep stall in Figure 13.

Fig. 23 Contribution to the pitching moment by q and $\dot{\alpha}$ for the deep stall in Figure 13.

Table 7 Identification and Validation MSE for the model presented in this paper and the model by van Ingen et al. [12].

Data	MSE model current paper	MSE model van Ingen et al. [12]	Difference [%]
Identification data			
Asymmetric stalls (12 stalls)	$4.50{\cdot}10^{-5}$	$1.82{\cdot}10^{-4}$	-75.2
Wings-level stalls (9 stalls)	$6.07{\cdot}10^{-5}$	$1.06{\cdot}10^{-4}$	-42.7
All identification data	$5.15{\cdot}10^{-5}$	$1.44{\cdot}10^{-4}$	-64.3
Validation data			
Stall 2	$3.93{\cdot}10^{-5}$	$4.36{\cdot}10^{-5}$	-9.92
Stall 6	$3.67{\cdot}10^{-5}$	$7.17{\cdot}10^{-5}$	-48.8
Stall 14	$4.36{\cdot}10^{-5}$	$2.69{\cdot}10^{-4}$	-83.8
Stall 19	$2.32{\cdot}10^{-5}$	$1.43{\cdot}10^{-4}$	-83.8
Stall 24	$1.08{\cdot}10^{-4}$	$8.45{\cdot}10^{-5}$	+28.4
All validation data	$4.89{\cdot}10^{-5}$	$1.11{\cdot}10^{-4}$	-55.9

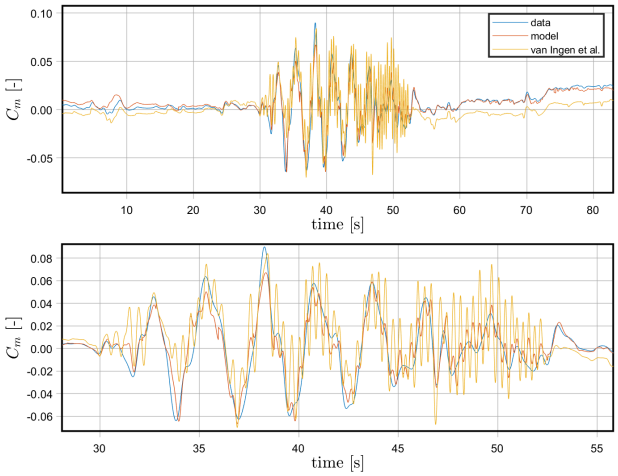

Fig. 24 Model fit on validation set 14 of full time trace (top) and close up stall maneuvers (bottom).

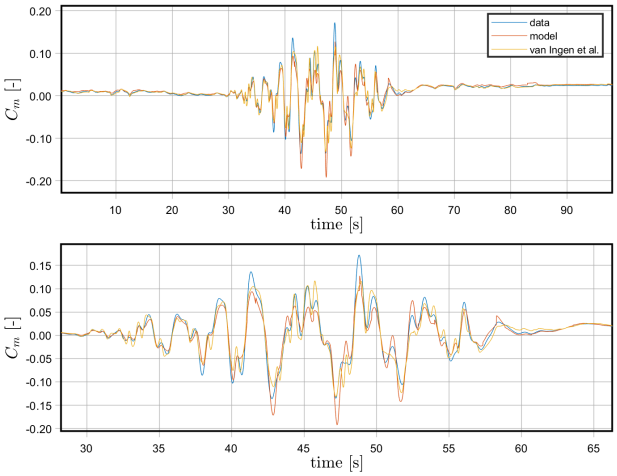

Fig. 25 Model fit on validation set 24 of full time trace (top) and close up stall maneuvers (bottom).

extremely noisy. This seems to be the direct result of the quasi-random inputs applied to the elevator. It is likely that the quasi-random inputs are too high in frequency, not allowing the pitching moment to adapt to the input. If that is indeed the case, only the bias applied to the control column exerts a direct influence on the pitching moment and the quasi random disturbances appear as noise in the signal since there is no correlated pitching moment response. The new model accounts for that with a drastic reduction in elevator effectiveness through $C_{m2_{\delta_e}}$. Whereas the nominal model reports $C_{m1_{\delta_e}} = -1.25$, the stall model reduces it by 0.965 to only -0.285. In stall 14 (Figure 24), the model improves over 83% on van Ingen's model mainly as a result of the latter's inability to model the elevator contribution.

The large modeling errors produced by the van Ingen model due to the elevator disturbances especially become evident when the inputs exceed a certain magnitude. Only stall sets 14 and 19 exceeded this apparent threshold, leading to an MSE improvement of 83.4 % compared to van Ingen et al. in both cases. This gives the impression that a nonlinear phenomenon might also be in effect. In a first attempt to account for the high frequency elevator inputs using the modeling methodology presented in this paper, a new set of candidates was added including elevator and elevator rate candidates modeled as functions of alpha by means of splines similar to C_{m2_q} and $C_{m2_{\dot{\alpha}}}$. At first glance, these $C_{m_{\delta_e}}(\alpha)$ and $C_{m_{\dot{\delta}_e}}(\alpha)$ functions do not solve the issue, and instead introduce overfitting issues. This strengthens the conjecture that the problem arises from the input design.

The model by van Ingen et al. outperforms the new model in one of the 5 validation sets, being set 24. Figure 25 shows the C_m time traces and model predictions. Although the new model picks up on variations in the pitching moment, it has trouble correctly predicting the C_m peaks, both positive and negative. Including more identification data with large pitching moment excursions should help reduce the deficit.

Finally, validation data and fits for the remaining three validation sets are shown in Figure 26-28.

VIII. Conclusion

This paper presents a novel aerodynamic model structure that can capture the nonlinear unsteady characteristics of the pitching moment during stall, especially aerodynamic damping, of the Cessna Citation II. Additionally, the model achieves global modeling capabilities in the sense that it is valid in stall as well as nominal flight conditions in combination with high physical interpretability. The model is meant to serve as an alternative to Kirchhoff-based models that are lacking with regard to those objectives. The model proposed is based on aerodynamic lag states to capture time varying effects. Furthermore, it is based on the linear stability derivative formulation that has been prevalent since the early days of aviation. It includes contributions identical to the nominal pitching moment model, augmented with correction terms that model deviations from linear attached flow in the nonlinear unsteady regime. To create the model a large pool of candidate regressor terms was defined out of which the best model terms were selected using Multivariate Orthogonal Function modeling. The combined effect of flow separation and the moving center of pressure is modeled by means of lag states of the angle of attack, where lags of 0.3 s, 0.07 s as well as the instantaneous angle of attack were included. Three lag states implies that the model picks up on information up to the second time derivative of the angle

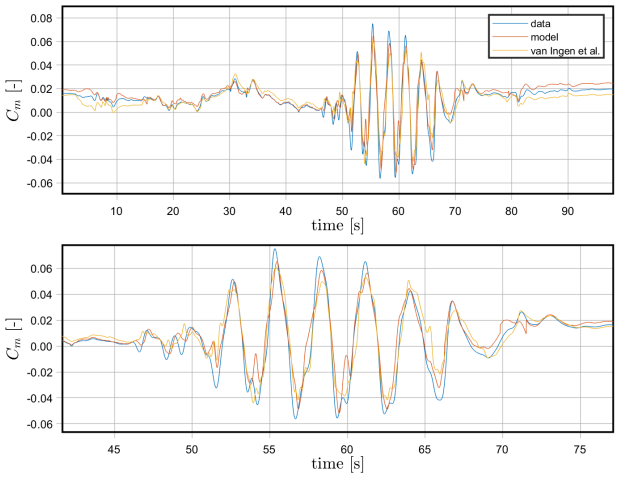

Fig. 26 Model fit on validation set 2 of full time trace (top) and close up stall maneuvers (bottom).

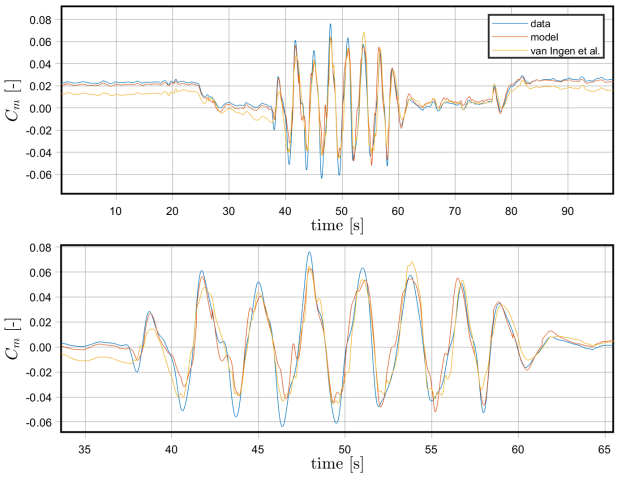

Fig. 27 Model fit on validation set 6 of full time trace (top) and close up stall maneuvers (bottom).

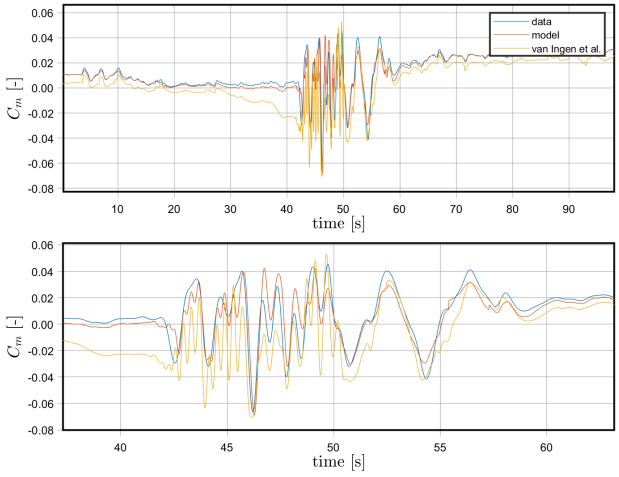

Fig. 28 Model fit on validation set 19 of full time trace (top) and close up stall maneuvers (bottom).

of attack. It is demonstrated how this model is sensitive to the frequency of the angle of attack time trace, and how it represents nonlinear and time-dependent aerodynamics. Furthermore, contributions were found for the pitch damping in stall for angles of attack over 5° and a downwash lag damping term for angles of attack over 8°. Additionally, a thrust coefficient parameter and a correction on the elevator effectiveness were found to be beneficial for the model fit. In terms of validation MSE, the new model provides an improvement of 55.9% over the Kirchhoff based pitching moment stall model by van Ingen et al. [12].

References

[1] "Safety Report 2019," Safety Report Edition 56, International Air Transport Association, Montreal, Quebec, Canada, 2020.

[2] "Federal Aviation Administration. Advisory Circular 120-109A - Stall Prevention and Recovery Training," Tech. rep., Federal Aviation Administration, 2015.

[3] "EASA. Certification specifications for aeroplane flight simulation training devices," Tech. Rep. CS-FSTD(A), European Aviation Safety Agency, 2018.

[4] Advani, S., and Field, J., "Upset Prevention and Recovery Training in Flight Simulators," Portland, US, 2011. https://doi.org/10.2514/6.2011-6698.

[5] J. R. Chambers, and S. B. Grafton, "Aerodynamic Characteristics of Airplanes at High Angles of Attack," *Journal of Aircraft*, 1977, pp. 1109–1115.

[6] Tobak, M., and Schiff, L. B., "On the formulation of the aerodynamic characteristics in aircraft dynamics," Techmical Report TR R-456, NASA, Moffet Field, California, USA, 1976.

[7] Klein, V., and Noderer, K. D., "Modeling of Aircraft Unsteady Aerodynamic Characteristics. Part I - Postulated Models," Technical Memorandum TM-109120, Langley Research Center, NASA, Hampton, Virginia, USA, 1994.

[8] Goman, M., and Khrabrov, A., "State-space representation of aerodynamic characteristics of an aircraft at high angles of attack," *Journal of Aircraft*, Vol. 31, No. 5, 1994, pp. 1109–1115. https://doi.org/10.2514/3.46618, URL https://doi.org/10.2514/3.46618, publisher: American Institute of Aeronautics and Astronautics _eprint: https://doi.org/10.2514/3.46618.

[9] Abramov, N., Goman, M., Khrabrov, A., and Soemarwoto, B., "Aerodynamic Modeling for Poststall Flight Simulation of a Transport Airplane," *Journal of Aircraft*, Vol. 56, 2019, pp. 1–14. https://doi.org/10.2514/1.C034790.

[10] Klein, V., "Modeling of Longitudinal Unsteady Aerodynamics of a Wing-Tail Combinat," Contractor Report CR-1999-209547, Langley Research Center, NASA, Hampton, Virginia, USA, 1999.

[11] Murphy, P., and Klein, V., "Estimation of Longitudinal Unsteady Aerodynamics of a Wing-Tail Combination from Wind Tunnel Data," *AIAA Atmospheric Flight Mechanics Conference and Exhibit*, American Institute of Aeronautics and Astronautics, Keystone, Colorado, 2006. https://doi.org/10.2514/6.2006-6154, URL https://arc.aiaa.org/doi/10.2514/6.2006-6154.

[12] van Ingen, J., de Visser, C. C., and Pool, D. M., "Stall Model Identification of a Cessna Citation II from Flight Test Data Using Orthogonal Model Structure Selection," *AIAA Scitech 2021 Forum*, American Institute of Aeronautics and Astronautics, 2021. https://doi.org/https://doi.org/10.2514/6.2021-1725.

[13] Fischenberg, D., "Identification of an unsteady aerodynamic stall model from flight test data," *20th Atmospheric Flight Mechanics Conference*, American Institute of Aeronautics and Astronautics, 1995. https://doi.org/10.2514/6.1995-3438, URL https://arc.aiaa.org/doi/10.2514/6.1995-3438.

[14] Mccroskey, W. J., "The Phenomenon of Dynamic Stall." Technical Memorandum, Ames research center, NASA, Moffet Field, California, USA, 1981.

[15] Khrabrov, A., Vinogradov, Y., and Abramov, N., "Mathematical Modelling of Aircraft Unsteady Aerodynamics at High Incidence with Account of Wing-Tail Interaction," AIAA Atmospheric Flight Mechanics Conference, Provedence, Rhode Island, USA, 2004.

[16] Corke, T., and Thomas, F., "Dynamic Stall in Pitching Airfoils: Aerodynamic Damping and Compressibility Effects," *Annual Review of Fluid Mechanics*, Vol. 47, 2015. https://doi.org/10.1146/annurev-fluid-010814-013632.

[17] Maine, R. E., and Iliff, K. W., "Maximum Likelihood Estimation of Translational Acceleration Derivatives from Flight Data," *Journal of Aircraft*, Vol. 16, No. 10, 1979, pp. 674–679. https://doi.org/10.2514/3.58588, URL https://arc.aiaa.org/doi/10.2514/3.58588, publisher: American Institute of Aeronautics and Astronautics.

[18] Jategaonkar, R. V., and Gopalratnam, G., "Two complementary approaches to estimate downwash lag effects from flight data," *Journal of Aircraft*, Vol. 28, No. 8, 1991, pp. 540–542. https://doi.org/10.2514/3.46060, publisher: American Institute of Aeronautics and Astronautics.

[19] Grauer, J. A., Morelli, E. A., and Murri, D. G., "Flight Test Techniques for Quantifying Pitch Rate and Angle of Attack Rate Dependencies," *Journal of Aircraft*, Vol. 54, No. 6, 2017.

[20] Morelli, E. A., "Global nonlinear aerodynamic modeling using multivariate orthogonal functions," *Journal of Aircraft*, Vol. 32, No. 2, 1995, pp. 270–277. https://doi.org/10.2514/3.46712.

[21] Klein, V., and Morelli, E. A., *Aircraft system identification - theory and practice*, AIAA education series, Vol. 2, Sunflyte Enterprises, Williamsburg, VA, USA, 2016. OCLC: 664103034.

[22] Carr, L. W., "Progress in analysis and prediction of dynamic stall," *Journal of Aircraft*, Vol. 25, No. 1, 1988, pp. 6–17. https://doi.org/10.2514/3.45534.

[23] Choudhry, A., Leknys, R., Arjomandi, M., and Kelso, R., "An insight into the dynamic stall lift characteristics," *Experimental Thermal and Fluid Science*, Vol. 58, 2014, pp. 188–208. https://doi.org/10.1016/j.expthermflusci.2014.07.006.

[24] Ericsson, L. E., and Reding, J. P., "Fluid mechanics of dynamic stall part I. Unsteady flow concepts," *Journal of Fluids and Structures*, Vol. 2, No. 1, 1988, pp. 1–33. https://doi.org/10.1016/S0889-9746(88)90116-8.

[25] McCroskey, W. J., McAlister, K. W., Carr, L. W., Pucci, S. L., Lambert, O., and Indergrand, R. F., "Dynamic Stall on Advanced Airfoil Sections," *Journal of the American Helicopter Society*, Vol. 26, No. 3, 1981, pp. 40–50. https://doi.org/10.4050/JAHS.26.40.

[26] Liiva, J., Davenport, F., Gray, L., and Walton, I., "Two-dimensional tests of airfoils oscillating near stall. Volume 1. Summary and evaluation of results," 1968.

[27] Higgins, R., Barakos, G., and Filippone, A., "A review of propeller stall flutter," *Aeronautical Journal*, Vol. 126, 2022. https://doi.org/10.1017/aer.2022.12.

[28] Carr, L. W., Mcalister, K. W., and Mccroskey, W. J., "Analysis of the development of dynamic stall based on oscillating airfoil experiments," Technical Note A-6674, NASA, Jan. 1977. URL https://ntrs.nasa.gov/citations/19770010056, nTRS Author Affiliations: NASA Ames Research Center NTRS Document ID: 19770010056 NTRS Research Center: Legacy CDMS (CDMS).

[29] Etkin, B., *Dynamics of Atmospheric Flight*, Dover Publications, 2000. URL https://app-knovel-com.tudelft.idm.oclc.org/kn/resources/kpDAF00013/toc.

[30] Morelli, E., Cunningham, K., and Hill, M., "Global Aerodynamic Modeling for Stall/Upset Recovery Training Using Efficient Piloted Flight Test Techniques," 2013. https://doi.org/10.2514/6.2013-4976.

[31] Van Horssen, L., De Visser, C. C., and Pool, D. M., "Aerodynamic Stall and Buffet Modeling for the Cessna Citation II Based on Flight Test Data," *2018 AIAA Modeling and Simulation Technologies Conference*, American Institute of Aeronautics and Astronautics, Kissimmee, Florida, 2018. https://doi.org/10.2514/6.2018-1167, URL https://arc.aiaa.org/doi/10.2514/6.2018-1167.

[32] van den Hoek, M., de Visser, C., and Pool, D., "Identification of a Cessna Citation II Model Based on Flight Test Data," *4th CEAS Specialist Conference on Guidance, Navigation and Control*, Warsaw, Poland, 2017.

[33] Morelli, E. A., "Nonlinear Unsteady Aerodynamic Modeling using Empirical Orthogonal Functions," Technical Memorandum TM–20210009593, Langley Research Center, NASA, Hampton, Virginia, USA, 2021.